UNIVERSIDAD AUTÓNOMA DE MADRID
ESCUELA POLITÉCNICA SUPERIOR

TRABAJO FIN DE MÁSTER

Análisis de dispositivos de microondas con simetrías de primer y segundo orden mediante el Método de los Elementos Finitos 2D

Máster Universitario en Ingeniería de Telecomunicación

Autor: Ginés García Contreras
Tutores: Juan Córcoles Ortega, Jorge A. Ruiz Cruz

FECHA: 21 de Junio, 2021

MICROWAVE 2D FINITE ELEMENT METHOD ANALYSIS FOR FIRST AND SECOND ORDER SYMMETRIC DEVICES

AUTHOR: Ginés García Contreras
DIRECTORS: Juan Córcoles Ortega, Jorge A. Ruiz Cruz

Radiofrecuencias: Circuitos, Antenas y Sistemas
Dpto. de Tecnología Electrónica y de las Comunicaciones
Escuela Politecnica Superior
Universidad Autonoma de Madrid
June 21st, 2021

Abstract

Resumen

Los dispositivos de microondas son la base sobre la cual se fundamentan los sistemas de comunicaciones, hoy en día omnipresentes como consecuencia del enorme crecimiento y popularización que han sufrido las Tecnologías de la Información (TI). Ámbitos como las comunicaciones inalámbricas ubicuas (como el 5G), el Internet de las Cosas (IoT, por sus siglas en inglés) y los sistemas de geolocalización (Galileo, GPS, GLONASS), así como otras recientes iniciativas privadas (Starlink de SpaceX, Proyecto Kuiper de Amazon) necesitan de nuevos dispositivos con capacidades y prestaciones potenciadas que atiendan las demandas de la industria. Entre las tecnologías más utilizadas en el ámbito de alta potencia y bajas pérdidas está la guía de onda, muy empleada, por ejemplo, en aplicaciones aeroespaciales. En el contexto de las antenas diseñadas en esta tecnología, también destacan las estructuras selectivas en frecuencia (FSS) y polarización (PSS), elaboradas mediante rejillas periódicas y capaces de ser fabricadas mediante manufacturación aditiva (impresión 3D).

Para el diseño y optimización de estos dispositivos de microondas predominan hoy en día las herramientas basadas en el diseño asistido por ordenador (CAD, en inglés). Estas herramientas, versátiles y potentes, permiten hacer el análisis electromagnético de las estructuras basadas en las tecnologías antes descritas y muchas otras, obteniendo una gran precisión en los resultados. En este ámbito, destaca el Método de los Elementos Finitos (FEM, por sus siglas en inglés), basado en la división de una estructura en secciones finitas, para las que se obtiene un resultado discretizado que es una aproximación del real. Esta técnica, a pesar de ser potente y general, y precisamente por ello, puede ser muy costosa computacionalmente.

En este proyecto, atendiendo a la demanda de crear herramientas de análisis más completas y eficientes, se ha tomado como punto de partida el Método de los Elementos Finitos, y se ha estudiado en casos particulares aplicados a guías de onda, FSS y PSS; tanto de análisis modal como de problemas de excitación, buscando optimizaciones que reduzcan el coste computacional y aporten información de interés basándose en las propiedades de simetría de dichas estructuras, tanto de primer como de segundo orden.

Palabras Clave

Método de los Elementos Finitos, guías de onda homogéneas, modos TE y TM, análisis modal, simetrías, polarización circular, FSS, PSS, dispositivos de microondas, dispositivos C_N.

Abstract

Microwave devices are the basis in which communication systems are founded. These components are nowadays omnipresent in all aspects of our lives due to the great growth and popularisation Information Technologies (IT) have experienced. Areas such as ubiquitous wireless communications (e.g. 5G), the Internet of Things (IoT) and positioning systems (Galileo, GPS, GLONASS), as well as other recent private initiatives (SpaceX's Starlink, Amazon's Project Kuiper) are in need of new devices with enhanced capabilities that satisfy the industry demands. Waveguides belong in the field on devices devised for high power transmission and low losses, which are used, as an example, in aerospace applications. In the context of antennas designed in this technology, Polarisation Selective Structures and Frequency Selective Structures (PSS and FSS, respectively), based on periodic meshes, are experiencing a popularity increase thanks to additive manufacturing (3D printing).

Nowadays, for the design and optimization of waveguide devices, the tools based on Computer Aided Design (CAD) are preferred. These versatile and powerful tools allow for electromagnetical analyses of the structures previously described and many others, obtaining great accuracy in the results. In this field, the Finite Element Method (FEM), based on the subdivision of a structure in finite regions for which the result is approximated, stands out over many others. This technique, although very general and powerful, can for that very reason be computationally demanding.

In this project, attending to the ever increasing demand of creating tailored and efficient tools for device analysis, the Finite Element Method has been taken as an starting point. Many particular cases regarding waveguides, FSS and PSS have been studied, concerning modal analysis and excitation problems, with the objective of finding optimizations that reduce the computational cost of simulating said structures and give additional information of interest based their geometrical symmetry properties, the focus being put in those of first and second order.

Key words

Finite Element Method (FEM), homogeneous waveguides, TE and TM modes, modal analysis, symmetries, circular polarisation, FSS, PSS, microwave devices, C_N devices.

Contents

List of Figures

List of Tables

1 Introduction

1.1 Project motivation

In recent decades Information Technology (IT) has seen an unprecedented growth thanks to the many innovations the extensive research and funding on the area has brought. In this ever-expanding field, communication systems play a fundamental role as they allow for an almost instantaneous transmission of information, regardless of how far away the interlocutors might be. At the heart of communications systems live microwave devices, which are the physical structures through which the information flows in the form of electromagnetic fields. Improvements in these structures allow engineers to build new, cutting-edge technology as an answer to the industry ever increasing demands. Microwave device designers are constantly challenged to build for better power efficiency, higher bandwidth, smaller dimensions and more versatility in their new products.

Because of the high constrains with which they work, it becomes very important to design microwave devices in an accurate, reliable and efficient way, to keep up with the advancements in fields such as the *Internet of Things* (IoT) [1], where millions of small antennas are being deployed, mobile communications such as the *Fifth Generation Communications* (5G) [2], that are empowering users with record levels of low latency and high bandwidth, and satellite communications, such as the European Global Navigation Satellite System (GNSS) *Galileo* [3], which is meant to bring geolocalization to the next generation of applications. Other recent ventures, such as SpaceX's Starlink [4], aim to provide internet access to millions of people via Low Earth Orbit satellites.

Microwave devices are expected to work in the millimetre-wave range, as small wavelengths allow for smaller devices and can coexist with older, lower-frequency systems (for the 5G network, 20 to 40 GHz bands have already been auctioned). To analyse them it is fundamental to use the tools that *Computer Aided Design* (CAD) [5] brings, which can be utilised for electromagnetical analysis of almost any structure. The Finite Element Method (FEM) [6, 7, 8] plays an important role in this field because of its versatility and good performance. The method on itself can be rather demanding computationally for complex simulations, and thus there are many techniques to improve its speed, such as the exploitation of their first or second-order symmetries, which is the main motivation of this work.

Recently, the analysis of higher-order symmetries such as twist symmetry (see Fig. 1.1a, a possible simplified version of a leaky wave antenna), which is a combination of translation and mirror symmetry; or glide symmetry, a combination of translation and rotation, in transmission media problems has regained the attention of the scientific community because of its prospective application to the analysis of a wide variety of devices [9, 10]. This has motivated researchers to further study how these geometrical properties influence the electromagnetic propagation in higher-order symmetrical devices, in an attempt to facilitate their analysis and to provide tools for a better understanding of their nature. This is crucial in waveguides devices, where the characterization of its modal spectrum is the starting point of any design. Moreover, for many analysis techniques [6], it is also required to compute a high number of modes, efficiently and precisely, and have them classified by modal symmetries.

This has motivated us develop a project that is about studying symmetries and applying geometrical properties to the calculus of the electromagnetic response of devices through 2D FEM to make it more efficient, so that it later may be translated to three dimensions or other applications, where the benefits are significantly more prominent.

1.2 Goals and approach

This work will focus on the study of diverse methods for the simulation of RF devices, including waveguides, waveguide devices and frequency selective structures (FSS) or polarisation selective structures (PSS), like the one shown in Fig. 1.1b, which works as a spacial filter that could be mounted over an antenna aperture. The Finite Element Method (FEM) will be the tool of choice to compute the electromagnetic response of all the geometries, because of its versatility and popularity in the RF community, as well as its proven accuracy. As many of the state-of-the-art devices have some kind of symmetry, generic formulations existing in the literature will be tailored to exploit these properties with efficient 2D formulations, understanding the steps and reasoning behind each of the changes. Also, continuing with the work presented in the *Trabajo Fin de Grado* (TFG) by the same author [11], we will work on obtaining a new, robust formulation for wavenumber computation in waveguides with discrete rotational symmetry (C_N), which will presumably have the advantages already foreseen in that work. As an example, the antenna in Fig. 1.1c, that can be suitable for radar applications, has both first and second order symmetry.

The approach will be both theoretical and practical, studying and constructing the formulations from different sources, and then verifying them and testing our theories by putting them into working code. All the computations related to FEM will be done using the open source library FEniCS [12, 13], primarily developed in C++, which has a C++ and Python API [14]. An implementation using open source tools has many advantages, the most important one being the possibility of publishing the code and not being dependent on software licenses and opaque, pre-compiled sources. The Python API was chosen having in mind the fast-prototyping philosophy of the language, which allows for very high level coding by giving up some performance. Other important libraries used in this project were NumPy [15], SciPy [16], Matplotlib [17], and the ARPACK linear algebra routines [18]. Although the scripts are written in Python, the most computationally demanding work is performed in either C++ or FORTRAN calls thanks to the interfaces given by the libraries and the Just-In-Time (JIT) compilation [19]. For displaying other results like what is shown in Fig. 1.1d, the visualization application Paraview [20] (also open source) was used, thanks its integration with FEniCS.

1.3 Methodology and work plan

To perform the proposed tasks, a relatively deep understanding of FEM is needed, mainly because some of the projected utilities are not implemented in the current libraries. Thus, first FEM will be dissected, studying every step of the process. Then, some relevant formulations for different problems will be analysed, as presented by various experts in the field. They will be tested and tailored to work more efficiently in first and/or second-order symmetric devices under a 2D FEM formulation. Finally, after gathering all this knowledge, a new 2D FEM formulation will be presented for C_N waveguides, putting together the analytical results previously obtained in the TFG and the strengths of the numerical computation.

Results will be shown for all formulations, studying the advantages and disadvantages of the ideas proposed, comparing the results between formulations. The majority of analysis will be done on the new C_N-FEM formulation, designed for waveguides with second-order rotational symmetries, which is the main innovation of this *Trabajo Fin de Máster*.

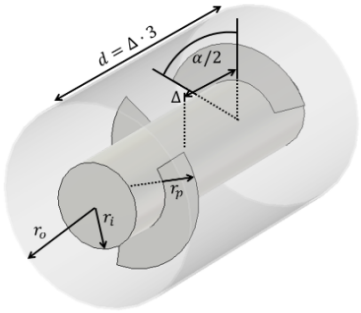

(a) Waveguide device with twist symmetry [9].

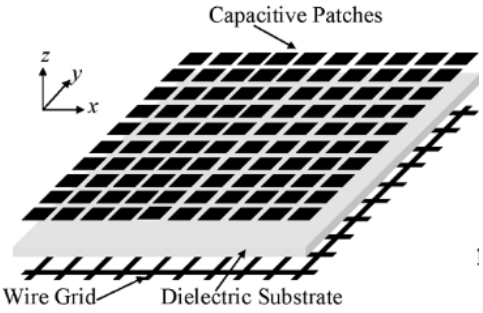

(b) Frequency selective structure [21].

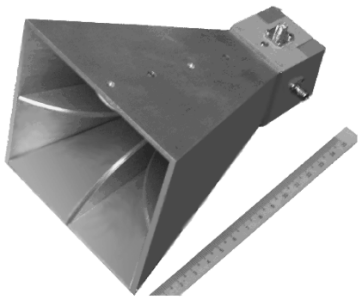

(c) A symmetric horn antenna [22].

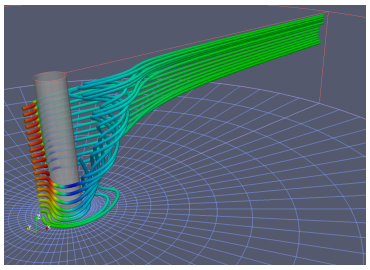

(d) CAD simulation visualization [20].

Figure 1.1: Project overview.

2

Introduction to the Finite Element Method and the FEniCS library

The Finite Element Method is a very versatile procedure used in a wide variety of engineering and physics areas such as thermodynamics, fluid theory and, most importantly for this project, electromagnetism. It is primarily employed to solve *Partial Differential Equations* or PDEs by approximating a desired unknown function with finite (discrete) elements.

2.1 The Finite Element Method

2.1.1 Overview

The Finite Element method consists on five basic steps that are performed regardless of the problem to be solved. Before step one, the subject must have the original problem properly characterized and discretized (this is referred in the following section as "step 0"). They are, namely:

1. Preprocessing: subdividing the region into finite elements.
2. Building element matrices: determining the functional on each element.
3. Assembling the global matrix: summing up the contributions from each element.
4. Solving the problem: a system of linear equations or a generalized eigenvalue problem.
5. Postprocessing: displaying results, computing derived values, etc.

In this Chapter we will discuss in more detail the most important aspects of each and every step. When doing frequency dependant simulations (all formulations studied in this work are intended for the Maxwell equations [23] in the frequency domain), we must iterate trough steps 2 to 5 for each of the desired frequencies.

2.1.2 Step 0: Problem formulation

Before applying FEM, one has to fist identify the *Partial Differential Equations* (PDEs) to be solved and their boundary conditions, mainly using well-known formulas derived from a physical analysis of the problem. Once done, the equations need to be reformulated as a variational problem. A general enunciation of a variational problem is to find a function $u \in V$ such that:

$$a(u, v) = L(v) \quad \forall v \in \hat{V}, \tag{2.1}$$

where V and $\hat{V}$ are referred, respectively, to as the trial function space and the test function space. Both spaces are restricted to be discrete to allow for a numerical approximation. a is called a *bilinear form* and L, a *linear form*, i.e.:

$$a : V \times \hat{V} \to \mathbb{R}, \tag{2.2}$$

$$L : \hat{V} \to \mathbb{R} \tag{2.3}$$

The variational problem is also referred to as *functional*. As rule of thumb, to obtain the variational formulation of a problem one multiplies the differential equations by a test function v, integrates the result over the domain and performs integration by parts on the second-order derivatives. When performing these tasks one obtains the so-called weak forms of the equations, which are satisfied on the average by enforcing that its weighted integral is zero. Because of this v can also be referred to as a *weighting function*. Although FEM is a variational technique, it is possible to derive equivalent formulations by using a projective approach or applying the *Weighted Residual Method* (WRM) using the Galerkin formulation [7], the latter being a commonly used tool for electromagnetic problems.

2.1.3 Step 1: Preprocessing

The preprocessing step is only related to geometry of the problem, and consists on dividing the structure in a set of nonoverlapping elements, such as triangles or tetrahedrons, typically using an automatic mesh generator. There are many available utilities that perform this process, both open source and privative. As it was not the objective of the project to dissect meshers in depth, it is only important to state the information a mesh generator should provide for further FEM computations. A mesh file should contain at least the following information [7]:

- Element vertices coordinates, also called *nodes*
- A connection matrix describing the mesh topology
- Labels for marking special nodes and elements (e.g. boundaries)

In general, a more dense mesh will yield better results and will require more resource-demanding computations. Some more advanced mesh generators have the ability to create a region-dependent mesh density based on the geometry under study, to improve accuracy while not dramatically increasing computation times.

2.1.4 Step 2: Building element matrices

Each element has associated an unknown function u, the same as in (2.1), which is approximated by a polynomial expression of a degree of choice, typically one or two. In each element this function can be expressed in the following manner:

$$u = \sum_{i=1}^{N} u_i \alpha_i \tag{2.4}$$

where N depends on the dimensions of the element and the polynomial order. α_i are referred to as *basis* or *shape functions* and take the value 1 at the node P_i and 0 at the nodes P_j, $i \neq j$. Values u_i are the unknowns to be obtained. When using scalar elements the most common element matrices used in FEM, and that will appear in almost all the formulations presented in future chapters are, with indices i, j, are:

$$S_{ij}^{(e)} = \iint_{\Omega_e} \nabla\alpha_i \cdot \nabla\alpha_j d\Omega, \tag{2.5}$$

$$T_{ij}^{(e)} = \iint_{\Omega_e} \alpha_i\alpha_j d\Omega. \tag{2.6}$$

The superscript (e) is put to emphasize that they have to be computed for every element in the whole domain Ω. Ω_e is the surface of the element (e) and α_i is the ith scalar function of the corresponding element. Note that in both expressions above it is implied that the trial functions are equal to the test functions, or, alternatively, the weighting functions are equal to the basis functions. This will be the case for all the problems discussed and is referred to as the *Galerkin formulation*. To further understand the nature of the base functions we will now discuss one of the simplest and most commonly used elements in FEM, the *Lagrange elements*.

The Lagrange element

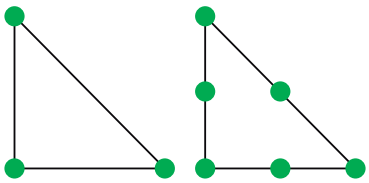

Figure 2.1: Lagrange elements of first (left) and second order (right) for a triangular element.

To define Lagrange elements, shown as dots in Fig. 2.1, it is first needed to exactly state what a finite element is. The starting point is that it is entirely defined by a triple $(T, \mathcal{V}, \mathcal{L})$ [24], where T is the domain of the finite element; the space $\mathcal{V}$ is a finite dimensional function space on T of dimension n; and $\mathcal{L} = \{l_1, l_2, ..., l_n\}$ are the sets of degrees of freedom, and a basis for the space of bounded linear functionals on $\mathcal{V}$. Lagrange elements live in the well-known Sobolev space H^1. They are defined for a polynomial order $q = 1, 2, ...$ with the parameters:

$$T \in \{interval, triangle, tetrahedron\}, \tag{2.7}$$

$$\mathcal{V} = \mathcal{P}_q(T), \tag{2.8}$$

$$l_k(v) = v(x_k), \quad k = 1, ..., n(q). \tag{2.9}$$

Here, $\mathcal{P}_q(T)$ refers to the space of polynomials of degree up to and including q on the domain T. Note that the degrees of freedom l_i are obtained by evaluating a function v at the point x_k. $\{x_k\}_{k=1}^{n(q)}$ is an enumeration of points in T defined by:

$$x = \begin{cases} k/q, \quad 0 \leq k \leq q, & T \text{ interval}, \\ (k/q, l/q), \quad 0 \leq k+l \leq q, & T \text{ triangle}, \\ (k/q, l/q, m/q), \quad 0 \leq k+l+m \leq q, & T \text{ tetrahedron}. \end{cases} \tag{2.10}$$

The set of points just presented is not the only possible option, although there must be a point on each of the vertices, $q-1$ points on each edge, and $(q-1)(q-2)/2$ points per face.

Points are placed based on the mesh structure. Finally, the dimension of the Lagrange finite element corresponds to the dimension of the complete polynomials of degree q on T:

$$n(q) = \begin{cases} q+1, & T \text{ interval}, \\ \frac{1}{2}(q+1)(q+2), & T \text{ triangle}, \\ \frac{1}{6}(q+1)(q+2)(q+3), & T \text{ tetrahedron}. \end{cases} \tag{2.11}$$

For the 2D FEM case, which is the one under study in this work, intervals and triangles will be used, but not tetrahedrons, as they only appear in 3-dimensional structures. Lagrange elements are the only ones used in this work.

Element transformation and numerical integration

One of the most used properties for the computation of element matrices shown in (2.6), (2.5) is using reference values for functions α_i and numerical integration, thus avoiding the need of integrating each element using its specific base functions, noted as, $\bar{\alpha}_i$ dependent on the mesh coordinates of its points. For the 2D case:

$$T_{ij} = \iint_{\Omega_e} \bar{\alpha}_i \bar{\alpha}_j dxdy = \int_{-1}^{1}\int_{-1}^{1} \alpha_i \alpha_j |\mathbf{J}| dudv, \tag{2.12}$$

$$S_{ij} = \iint_{\Omega_e} \nabla\bar{\alpha}_i \cdot \nabla\bar{\alpha}_j dxdy = \int_{-1}^{1}\int_{-1}^{1} \left[(\nabla_{u,v}\alpha_i)^T \left(\mathbf{J}^{-1}\right)^T\right] \cdot \left[\mathbf{J}^{-1}\nabla_{u,v}\alpha_j\right] |\mathbf{J}| dudv. \tag{2.13}$$

where $\mathbf{J}$ is the Jacobian of the transformation, that for the 2D case is defined as:

$$\mathbf{J} = \begin{bmatrix} \frac{\partial x}{\partial u} & \frac{\partial y}{\partial u} \\ \frac{\partial x}{\partial v} & \frac{\partial y}{\partial v} \end{bmatrix} \tag{2.14}$$

The integrals are simplified if the Jacobian is not a function of (u, v). As an example, for a segment $[0, 1]$ characterized with Lagrangian elements of order $q = 2$ ($n(q) = 3$) we have the following normalised base functions α_i. It is easy to see that they take the value 1 in their respective points $P_i = \{0, 1/2, 1\}$ and 0 in every other P_j, $i \neq j$.

$$\alpha_1(u) = -(1 - 2(1-u))(1-u) \tag{2.15}$$

$$\alpha_2(u) = 4(1-u)u \tag{2.16}$$

$$\alpha_3(u) = -(1-2u)u \tag{2.17}$$

Gaussian or numerical integration may be used with the presented base functions to obtain the values needed for matrices $\mathbf{S}$ and $\mathbf{T}$ (in this case, for a segment). This is performed by evaluating the functions in predefined points and then multiplying them by constant weights. As an example, a 3-point numerical integration is performed using the points $\hat{x} = \{0, \sqrt{0.6}, -\sqrt{0.6}\}$ and the weights $w = \{8/9, 5/9, 5/9\}$, and guarantees an exact result for functions with a maximum polynomial order of $5 > 4$, which is the maximum order of the polynomials obtained when multiplying the functions (2.15) to (2.17). Note that this method is meant for a segment in the interval $[-1, 1]$, and so points from u need to be properly scaled and translated. Element transformation and numerical integration are used in Chapter 5.

2.1.5 Step 3: Assembling the global matrix

After obtaining the element matrices, the global matrix must be assembled. This is performed by summing up the contributions from each element into a matrix with a global ordering scheme. This global matrix has the property of having a sparse structure, because the number of nonzero entries of row i is equal to the number of DOFs directly connected to each other. Because of this the memory storage and CPU usage can be greatly reduced in comparison with using dense matrices. When assembling the global matrices, ordering techniques may be used to speed up and further optimize operations to be performed with them. It is at this stage where Dirichlet and other boundary conditions such as *Periodic Boundary Conditions* (PBC), discussed in Section 2.2 are usually applied.

2.1.6 Steps 4 and 5: Solving the problem and postprocessing

Once the global matrices have been assembled and the boundary conditions applied, the only step that is left is solving the entire problem, which usually is a system of linear equations or a generalized eigenvalue problem, though in some cases it can be a polynomial eigenvalue problem or a nonlinear eigenvalue problem. There are many solvers available for these tasks, some of them open source, with very efficient implementations and the ability to paralelize the calculus and exploit sparse matrix properties. The solver was not an object of study of this project and it will not be discussed any further.

Finally, the postprocessing aspect has, in general, nothing to do with pure FEM and greatly differs from application to application. In spite of this, most of the times it is useful to reuse some of the tools natively integrated in FEM suites such as numerical differentiation to obtain some derivative results that may be used for visualization purposes or as input data for other systems.

2.2 Boundary conditions and symmetries in FEM

Before discussing how to work with symmetries conditions in FEM, let us enumerate the most commonly used boundary conditions (BCs), summed up in Table 2.1, where "eq." means *equivalent*.

FEM Name	TE eq.	TM eq.	Symmetry order	Effect
Dirichlet BC	PMC	PEC	First	Creates odd functions
Neumann BC	PEC	PMC	First	Creates even functions
Periodic BC	Field periodicity		Second	Imposes a phase shift
Absorbing BC	Excitation/scattering		n/a	Forces/captures a field expression

Table 2.1: Most common types of boundary conditions.

In Table 2.1, note that the *symmetry order* and *effect* columns only apply when the BCs are correctly enforced in symmetrical problems. The first two boundary conditions are commonly applied to the edges of the structure when working with TE and TM modes [25], respectively. This is because their eigenfunctions ψ have to fulfil either of the following boundary conditions

in the perfect conductor facets, in the case of TM modes:

$$\psi|_c = 0 \quad \text{for Dirichlet} \tag{2.18}$$

$$\left.\frac{\partial \psi}{\partial n}\right|_c = 0 \quad \text{for Neumann,} \tag{2.19}$$

where c is the contour along which it will be imposed. The first one is associated with a Perfect Electric Conductor (PEC) in TM modes and Perfect Magnetic Conductor (PMC) in TE modes, and is also called the Dirichlet boundary condition. It can be enforced by removing the DOFs corresponding the points where one wishes to impose it. The second one is referred to as a Neumann or *natural* boundary condition and is associated with PMC and PEC for TM and TE modes, respectively, and it does not need any changes to be performed on the system of equations to be enforced, hence the name. Looking at the expressions, we can make use of these conditions in symmetric problems by appropriately imposing either one of them in the reflection axis. In general, imposing a Dirichlet BC will yield an odd function (because the result has to be derivable and pass through 0) and a Neumann BC an even function, because of the derivative being 0 at the reflection axis and the problem being symmetric.

For second-order symmetries in electromagnetics, Periodic Boundary Conditions (PBCs) are used. They enforce field periodicity by establishing a complex-valued relationship for the unknown function ψ in certain facets, such as:

$$\psi(u - T_u, v - T_v) = \psi(u, v) e^{-j(\theta_u + \theta_v)}. \tag{2.20}$$

where $\theta_u \propto T_u$ is a phase shift typically directly related to the spatial difference. The boundary where conditions are imposed is called the *slave* boundary and the the reference from which they are taken is called the *master* boundary [26, 27]. There are three equivalent methods for imposing PBCs:

- Sum the rows of the DOFs of the slave boundary with the phase difference into the master boundary and set the slave boundary rows to 0 (except for the diagonals, which are set to 1)
- Sum the rows and columns of the slave boundary into the master boundary taking into account the phase difference and remove the nodes corresponding to the slave boundary
- Use a projection matrix to establish the relation between the master and slave boundaries or all the nodes in the system.

The first method finds issues with the possible matrix symmetric properties (i.e., $A = A^H$, where H refers to the Hermitian or complex conjugate transpose operation). This is not desirable, especially when dealing with eigenvalue problems. The second one does not, but is still limited to meshes with aligned nodes at the boundaries. The third approach, although the slowest because implies the use of matrix multiplication, can be used for non-matching meshes at the boundaries. The second and third procedures can be combined to speed up the process while being able to use non-matching meshes. Periodic boundary conditions will be discussed in great detail in Chapter 4, and especially, in Chapter 5.

Finally, absorbing boundary conditions are generally not explicitly related to symmetries, but can produce symmetric results depending on their shape. Even if the problem is symmetric geometrically-wise, these boundary conditions can break the symmetry of the result, thus it is very important to consider their symmetries. Absorbing BCs appear in Chapters 3 and 4.

2.3 FEniCS, an open source PDE solver

To achieve the project goals, a high-level library for solving PDEs was used as a starting point, in this case FEniCS [14], which has an application program interface (API) available for Python and C++ programming, from which the former was selected. FEniCS serves like an interface between the analytical and numerical world, simplifying from the programmer's perspective some of the most time-consuming procedures, such as node ordering and matrix assembling. Among the advantages of FEniCS, the most important ones that influenced our decision on choosing it were:

- Transparency from the programmer's perspective when using different types of elements.
- Transparency from the programmer's perspective when using different kinds of interpolating functions.
- Intuitive variational problem implementation thanks to the *Unified Form Language* (UFL).
- Easy assembly of global matrices and consistent node ordering.
- Built-in tools for postprocessing.

Currently, FEniCS supports only triangular elements, which were suitable enough for our goals. Also, because of the tailoring that was needed for this project, only triangular elements were really a viable option for the final implementations. FEniCS also has an library of a wide variety of finite elements, but Lagrange elements were the only ones needed for the proposed implementation. The order of interpolating functions can be set to an arbitrary positive integer, although it was later limited to up to 2 because of the need of low-level programming some of the utilities.

The seamless assembly of element and global matrices is the most important advantage of FEniCS, since it takes care of translating expressions from variational problems defined with UFL into matrices and using consistent node ordering. Simple boundary conditions such as Dirichlet's can also be easily applied using FEniCS. For displaying results, the most practical way of visualization is achieved by saving the data in a Paraview [20] file or in a NumPy [15] (Python's most popular vectorial calculus library) array along with the DOF locations. Although the library saves a lot of work, it has some important disadvantages that became very noticeable during the duration of the project:

- The built-in mesher is rudimentary.
- Complex algebra is not supported.
- Periodic boundaries are very limited.
- Rotational boundary conditions are not implemented.
- No backwards compatibility
- Poor documentation.

The first problem can be solved by using other not built-in meshers, such as the more powerful *gmsh* (also open-source). Despite this, some compatibility issues still were found when importing meshes, even with standardised formats. In the end, the FEniCS-oriented Python library *mshr* was enough to perform the desired tasks. The second item is a very important limitation of FEniCS, because it *de facto* prevents some basic electromagnetical procedures to be performed.

It is possible to work around this limitation by duplicating matrices in the code representing, respectively, the real and imaginary parts, tough it was found impossible to establish periodic boundary conditions that took into account complex relationships.

These periodic boundaries, which were a very important part of the project, can only be established for values of the same matrix, and work in an opaque way. For this reason, they were implemented manually. For the last point, rotational boundary conditions are virtually impossible to implement using only FEniCS functions, and they were also taken to practice by manually manipulating the matrices. This was expected since it was one of the main innovations that this project presented.

FEniCS has suffered many significant changes since its first releases (it comes from an aggregate of other libraries). This means some of the older documentation is error-inducing and deprecated, since the library has no guaranteed backwards compatibility. As the last version has very little written documentation available other than the one automatically generated, finding working methods and functions was a challenge that was only possible to overcome thanks to the existing users' questions and answers in the dedicated forums and the method of trial and error.

3

E and H-plane FEM formulation

In the following chapters, a wide variety of approaches to the use of FEM in electromagnetics will be discussed. First, in this Chapter, the H and E plane [28] cases for hollow rectangular waveguide devices will be studied, starting from the formulation presented in [7]. Then, in Chapter 4, we introduce a formulation for a second-order symmetry problem based on [8], which is the scattering of a periodic structure. Finally, we apply this knowledge to waveguide cross-sections in Chapter 5, obtaining a new formulation that exploits first and second-order symmetries.

3.1 E and H-plane case for rectangular waveguides

E and H-plane devices are based on rectangular waveguides. They can be found, for instance, in [28] for conforming filters, transformers, etc. in many high-frequency communication systems, especially for high-power, as in satellite communications. In these devices only the waveguide's width or height changes, making it possible for the Maxwell equations involved to be solved with a 2D approach in the structure. The formulation presented is referred to as a hybrid method, because it combines the FEM numerical solution with analytic absorbing boundary conditions at the ports. A generic H and E-plane structure can be inspected in Fig. 3.1.

3.1.1 H-plane

Thanks to the assumption that only the TE_{10} propagates at the operating frequency, the field E_y may be expressed as a function of x in each port k (see Fig. 3.1a), following the formulation presented in [7]. It is assumed the excitation comes from port j, and thus the electric field $E_{y_{wg}}$ at each of them is:

$$E_{y_{wg}}^{(k)} = \delta_{kj} e_1^{(j)}(x^{(j)}) e^{j\beta_1^{(j)} z^{(j)}} + \sum_{m=1}^{\infty} B_m^{(k)} e_m^{(k)}(x^{(k)}) e^{-j\beta_m^{(k)} z^{(k)}}, \tag{3.1}$$

$$j\omega\mu_0 H_{x_{wg}}^{(k)}(x^{(k)}) = \frac{\partial E_{y_{wg}}^{(k)}}{\partial z^{(k)}}, \tag{3.2}$$

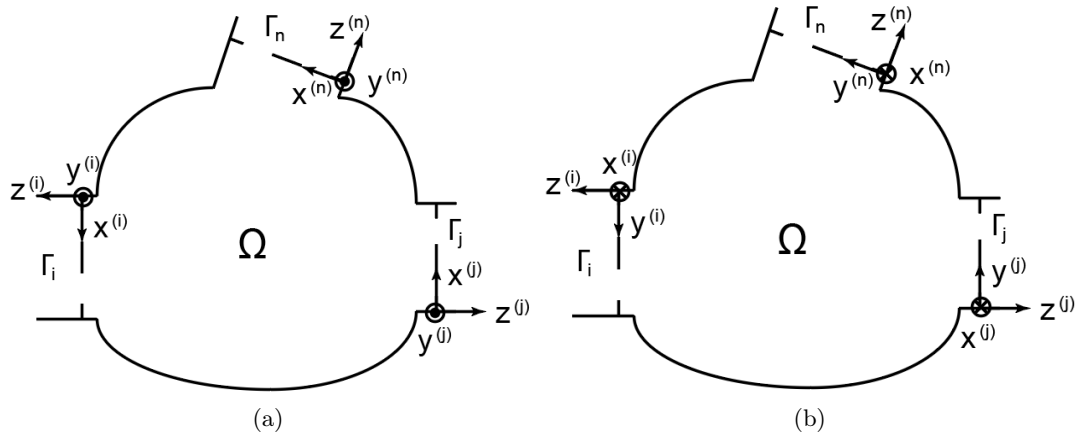

Figure 3.1: H (left) and E (right) plane generic geometry with n ports.

where β_m is the propagation constant, defined below; δ_{kj} is Kronecker's delta and B_m are unknown complex amplitudes. Obtaining the field $H_{x_{wg}}$ is done by computing the partial derivative of the E field along the z axis; ω is the angular frequency and μ_0 the vacuum magnetic permeability. Because of the problem topology, E_y and H_x are the only two components of the the total electromagnetic field [7]. Although excitation with mode TE_{10} is assumed, this formulation allows for the excitation to be any $\mathrm{TE}_{\mathrm{m0}}$ mode, given that:

$$e_m^{(k)}(x^{(k)}) = \frac{2}{a^{(k)}b}\sqrt{\frac{k_0 Z_0}{\beta_m^{(k)}}}\sin\left(\frac{m\pi}{a^{(k)}}x^{(k)}\right), \tag{3.3}$$

where Z_0 is the free-space characteristic impedance and $k_0 = \omega/\sqrt{\mu_0\epsilon_0}$, where ϵ_0 is the vacuum electric permittivity. The propagation constant β_m is also defined in each port as, where $k_{t_m}^{(k)} = m\pi/a^{(k)}$:

$$\begin{cases} \beta_m^{(k)} = \sqrt{k_0^2 - k_{t_m}^{(k)2}} & \text{for} \quad k_0^2 \geq k_{t_m}^{(k)2}, \\ \beta_m^{(k)} = -j\sqrt{k_{t_m}^{(k)2} - k_0^2} & \text{for} \quad k_0^2 < k_{t_m}^{(k)2}. \end{cases} \tag{3.4}$$

The perfect electric wall boundary condition $E_y = 0$ (Dirichlet) must be enforced in the edges of the structure not corresponding to ports. The H-plane problem can then be reduced to the following equations using the Weighted Residual Method (WRM). The first one is the excitation equation:

$$\int_{\Gamma_k} W E_y d\Gamma_k = \int_{\Gamma_k} W E_{y_{wg}}^{(k)} d\Gamma_k, \quad k = 1, ..., N, \tag{3.5}$$

where W is the weighting function and E_y is the unknown function. This equation states that the field at the ports must match the excitation stated in (3.1). The second one can be seen as the scattered field equation

$$\iint_\Omega \nabla_t W \cdot \frac{1}{\mu_r}\nabla_t E_y d\Omega - k_0^2 \iint_\Omega \epsilon_r W E_y d\Omega - \sum_{k=1}^{N}\int_{\Gamma_k} W \frac{\partial E_{y_{wg}}^{(k)}}{\partial z^{(k)}} d\Gamma_k = 0. \tag{3.6}$$

where ϵ_r, μ_r are, respectively, the relative permittivity and permeability. Please note that the dielectric could be inhomogeneous, or, for homogeneous dielectric, these terms could go out of the integral. The first two terms of this equation come from the Helmholtz equation, and the last one from the absorbing boundary conditions at the ports. These equations may be translated directly to the FEM numerical solution, which will be shown along the E-plane formulation in section 3.1.3.

3.1.2 E-plane

The E-plane case (see Fig. 3.1b) can be studied in an analogous way to the H-plane case, though in this case the method will solve the field for the component h_x. Instead of expressing the incident and scattered fields in terms of $\mathrm{TE_{m0}}$, $\mathrm{LSE^x{}_{1n}}$ modes [29] will be used, in the following way, with the unknown amplitudes $B_n^{(k)}$:

$$h_{x_{wg}}^{(k)(y^{(k)})} = \delta_{kj} h_0^{(j)}(y^{(j)}) e^{j\beta_0^{(j)} z^{(j)}} - \sum_{n=0}^{\infty} B_n^{(k)} h_n^{(k)}(y^{(k)}) e^{-j\beta_n^{(k)} z^{(k)}}. \tag{3.7}$$

The propagation constant β_n will be different from the H-plane case since the expansion was done in a different set of modes. Other than that, constants have the same meaning as in the previous section. Here $h_n^{(k)}$ refers to the orthonormal modal function of the $\mathrm{LSE^x{}_{1n}}$ modes. Note that in this case $n = 0, 1, ...$, and that any $\mathrm{LSE^x{}_{1n}}$ mode could, in theory, be used for the excitation.

$$h_n^{(k)}(y^{(k)}) = \frac{2}{\sqrt{1+\delta_{0n}}} \sqrt{\frac{2Z_0}{ab^{(k)} k_0 \beta_n^{(k)} \left(k_0^2 - \left(\frac{\pi}{a}\right)^2\right)}} \cos\left(\frac{n\pi}{b^{(k)}} y^{(k)}\right). \tag{3.8}$$

The propagation constant at each port k is a function of n, in this case:

$$\begin{cases} \beta_n^{(k)} = \sqrt{k_0^2 - k_{t_n}^{(k)2}} & \text{for} \quad k_0^2 \geq k_{t_n}^{(k)2}, \\ \beta_n^{(k)} = -j\sqrt{k_{t_n}^{(k)2} - k_0^2} & \text{for} \quad k_0^2 < k_{t_n}^{(k)2}. \end{cases} \tag{3.9}$$

where $k_{t_n}^2 = \left(\frac{\pi}{a}\right)^2 + \left(\frac{n\pi}{b^{(k)}}\right)^2$. After applying the WRM, the E-plane case can be stated in two equations very similar to the ones presented in the H-plane case, with the unknown function being h_x instead of E_y. The excitation equation states the amplitudes must match some set values at the ports:

$$\int_{\Gamma_k} W h_x d\Gamma_k = \int_{\Gamma_k} W h_{x_{wg}}^{(k)} d\Gamma_k, \quad k = 1, ..., N. \tag{3.10}$$

The scattered field equation matches the Helmholtz equation with the absorbing boundary conditions:

$$\iint_{\Omega} \nabla_t W \cdot \nabla_t h_x d\Omega - k_t^2 \iint_{\Omega} W h_x d\Omega - \sum_{k=1}^{N} \int_{\Gamma_k} W \frac{\partial h_{x_{wg}}^{(k)}}{\partial z^{(k)}} d\Gamma_k = 0. \tag{3.11}$$

Note that in this case Neumann boundary conditions must be set at the edges of the structure not corresponding to the ports, instead of the Dirichlet BCs that were imposed on the H-plane case.

3.1.3 Numerical implementation for the H and E-plane cases

The formulation presented in the previous sections may be expressed as a linear system of equations:

$$\begin{bmatrix} \mathbf{C} & \mathbf{F} \\ \mathbf{A} & \mathbf{D} \end{bmatrix} \begin{bmatrix} \mathbf{b} \\ \mathbf{u} \end{bmatrix} = \begin{bmatrix} \mathbf{u}'_{inc} \\ \mathbf{u}_{inc} \end{bmatrix} \tag{3.12}$$

where $\mathbf{C}$, $\mathbf{F}$, $\mathbf{A}$, $\mathbf{D}$ are matrices and $\mathbf{b}$, $\mathbf{u}$, $\mathbf{u}_{inc}$, $\mathbf{u}'_{inc}$ are vectors whose entries will be now enunciated. $\mathbf{b}$ is the vector of the unknown amplitudes B_m or B_n and $\mathbf{u}$ is the scattered field E_y

or h_x. The FEM matrix for the functional, related to the weak form of the Helmholtz equation is referred as **F** and is, for the H and E-plane cases respectively:

$$F_{ij}^{h} = \frac{1}{\mu_r} \iint_{\Omega} \nabla_t \alpha_i \cdot \nabla_t E_y d\Omega - k_0^2 \epsilon_r \iint_{\Omega} \alpha_i E_y d\Omega, \tag{3.13}$$

$$F_{ij}^{e} = \iint_{\Omega} \nabla_t \alpha_i \cdot \nabla_t h_x d\Omega - k_0^2 \mu_r \epsilon_r \iint_{\Omega} \alpha_i h_x d\Omega. \tag{3.14}$$

Matrix **C** is associated with the term of the partial derivative of the field a the ports, and its entries take the form:

$$C_{k_{im}}^{h} = j\beta_m^{(k)} \int_{\Gamma_k} \alpha_i e_m^{(k)} d\Gamma_k, \tag{3.15}$$

$$C_{k_{in}}^{e} = j\beta_n^{(k)} \int_{\Gamma_k} \alpha_i h_n^{(k)} d\Gamma_k. \tag{3.16}$$

Note that the propagation constant is different from the E and H plane cases, and that $m = 1, ..., \infty$ and $n = 0, ..., \infty$. Because infinite terms cannot be taken into account the sum must be truncated to the first M terms. Matrix **D** is associated with the boundary condition of the field at each of the ports:

$$D_{k_{mj}}^{h} = \int_{\Gamma_k} \sin\left(\frac{m\pi}{a^{(k)}} x^{(k)}\right) \alpha_j^{(k)} d\Gamma_k, \tag{3.17}$$

$$D_{k_{mj}}^{e} = \int_{\Gamma_k} \cos\left(\frac{n\pi}{b^{(k)}} y^{(k)}\right) \alpha_j^{(k)} d\Gamma_k. \tag{3.18}$$

A is a diagonal matrix associated with the normalising factor of each unknown amplitude in **b**. Normalisation constants are needed for the parameters in **b** to be $|b_i| \leq 1$ and for each k mode to be properly scaled.

$$A_{k_{mm}}^{h} = -\sqrt{\frac{a^{(k)}}{b}} \sqrt{\frac{k_0 Z_0}{\beta_m^{(k)}}}, \tag{3.19}$$

$$A_{k_{nn}}^{e} = -\frac{1}{\sqrt{1+\delta_{n0}}} \sqrt{\frac{a}{b^{(k)}}} \sqrt{\frac{2Z_0}{k_0 \beta_n^{(k)} \left(k_0^2 - \left(\frac{\pi}{a}\right)^2\right)}}. \tag{3.20}$$

The independent terms are associated with the incoming field or amplitude, first the amplitude $\mathbf{u}_{inc}$, which is obtained by integrating the field at the port l:

$$u_{inc,k_1}^{h} = \delta_{kl} \sqrt{\frac{a^{(l)}}{b}} \sqrt{\frac{k_0 Z_0}{\beta_1^{(l)}}}, \quad E_{km} = 0, \tag{3.21}$$

$$u_{inc,k_1}^{e} = \frac{\delta_{kl}}{\sqrt{1+\delta_{n0}}} \sqrt{\frac{a}{b^{(l)}}} \sqrt{\frac{2Z_0}{k_0 \beta_0^{(l)} \left(k_0^2 - \left(\frac{\pi}{a}\right)^2\right)}}, \quad E_{kn} = 0. \tag{3.22}$$

Finally the derivative of the incoming field $\mathbf{u}'_{inc}$ has the following entries in each index i:

$$u_{inc,k_i}^{\prime e} = j\beta_1^{(l)} \delta_{kl} \int_{\Gamma_k} \alpha_i e_1^{(l)} d\Gamma_k, \tag{3.23}$$

$$u_{inc,k_i}^{\prime h} = j\beta_0^{(l)} \delta_{kl} \int_{\Gamma_k} \alpha_i h_0^{(l)} d\Gamma_k. \tag{3.24}$$

Assuming the same number of modes is simulated on each port, and that we have K ports, the dimension of each of the matrices can be seen in Table 3.1, where N_{dof} is the number of DOFs in the problem. One possible way of solving this system is obtaining first $\mathbf{F}^{-1}$, which has to be of dimensions $N_{dof} \times N_{dof}$. Then it is possible to compute:

$$\mathbf{b}_r = \mathbf{u}_{inc} - \mathbf{D}\mathbf{F}^{-1}\mathbf{u}'_{inc}, \tag{3.25}$$

$$\mathbf{B}_l = \mathbf{A} - \mathbf{D}\mathbf{F}^{-1}\mathbf{C}, \tag{3.26}$$

$$\mathbf{B}_l\mathbf{b} = \mathbf{b}_r. \tag{3.27}$$

Depending on the solver it may be better to calculate the partial results $\mathbf{F}^{-1}\mathbf{u}'_{inc}$ and $\mathbf{F}^{-1}\mathbf{C}$ instead of $\mathbf{F}^{-1}$. Using this approach only the amplitudes $\mathbf{b}$ are obtained. If the field in the interior is required, the vector $\mathbf{u}$ can be obtained by substituting $\mathbf{b}$ in either of the equations in (3.12).

Matrix	$\mathbf{A}$	$\mathbf{D}$	$\mathbf{C}$	$\mathbf{F}$	$\mathbf{u}_{inc}$	$\mathbf{u}'_{inc}$	$\mathbf{b}$	$\mathbf{u}$
Rows	$M \times K$	$M \times K$	N_{dof}	N_{dof}	$M \times K$	N_{dof}	$M \times K$	N_{dof}
Columns	$M \times K$	N_{dof}	$M \times K$	N_{dof}	1	1	1	1

Table 3.1: Matrix dimensions for the H and E-plane linear system of equations.

3.1.4 Tailoring the formulation for first-order symmetries

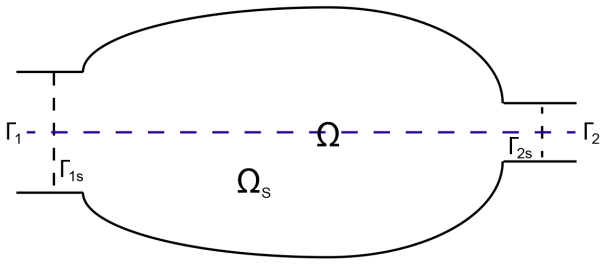

Figure 3.2: Symmetric 2-port H or E-plane device.

To tailor the formulation to withstand first order symmetries we consider the case of a two-port symmetric device along the horizontal axis such as the one presented in Fig. 3.2. Axis will be set the same way they are shown in Fig. 3.1 depending on the problem. Note that the ports either are halved or not affected at all when the symmetry is imposed. To understand the boundary conditions for each case first we look at the forcing vector $\mathbf{u}_{inc}$, which was based on, for the H and E-plane cases:

$$e_m^{(k)}(x^{(k)}) = \frac{2}{a^{(k)}b}\sqrt{\frac{k_0 Z_0}{\beta_m^{(k)}}}\sin\left(\frac{m\pi}{a^{(k)}}x^{(k)}\right) \tag{3.28}$$

$$h_n^{(k)}(y^{(k)}) = \frac{2}{\sqrt{1+\delta_{0n}}}\sqrt{\frac{2Z_0}{ab^{(k)}k_0\beta_n^{(k)}\left(k_0^2 - \left(\frac{\pi}{a}\right)^2\right)}}\cos\left(\frac{n\pi}{b^{(k)}}y^{(k)}\right) \tag{3.29}$$

Observing these expressions it can easily be seen that e_m is an even function when m is odd (centered in the reflection axis) and an even function when m is odd. The excitation vector, which will typically be e_1, will then impose a PMC boundary condition in the symmetry axis. The opposite can be said about h_n, which is odd when n is even and even when n is odd. Because

the forcing incident field is h_0, then PMC boundary conditions will have to be enforced in this case as well.

If PMC boundary conditions are to be enforced in the symmetry axis, then when simulating half the modes will have to be skipped, i.e., all the modes with m even and n odd, because they violate this condition. Indeed, these modes are not excited when the problem is symmetric.

Finally, we must tailor the equation $\mathbf{Ab} + \mathbf{Du} = \mathbf{u}_{inc}$. As said before, this equation was associated with the magnitude of the field at the ports. Because the magnitude has been halved due to imposing the symmetry, coefficients corresponding to halved ports in $\mathbf{A}$ and $\mathbf{U}$ must be divided by 2. Equation $\mathbf{Cb}+\mathbf{Fu} = \mathbf{u}'_{inc}$ is not to be changed since it only imposes the conditions on the derivative of the incident field. In conclusion, the steps to be performed are:

1. Impose Neumann boundary conditions (PMC) in the symmetry axis
2. Simulate only odd modes for the H-plane case and even modes for E-plane case
3. Divide by 2 the coefficients in $\mathbf{A}$ and $\mathbf{u}_{inc}$

If the device has more than two ports, some may be halved and some may not be depending on the geometry. It is important to note that if the port where the excitation comes from is duplicated, then the principal mode will be fed through mode than one port, and coefficients $\mathbf{b}$ will not be accurate unless a technique like Bartlett's theorem is applied to compute the parameters. In these kinds of problems, though, Bartlett is only needed when the ports' required parameters are outside the longitudinal symmetry axis

3.2 H and E-plane devices

3.2.1 H-plane

To show how the formulation tailoring works a simple Chevychev H-plane filter has been simulated and their results compared with an analytical method, called Mode-Matching [30], that is based on the modelling of waveguide discontinuities. This filter has been modelled using cavities and irises, an can be seen in Fig. 3.4a. The dimensions of each of the sections is shown in Table 3.2, where H means *height*, W, *width*, and L, *length*.

H-plane filter, H=7.9mm													
W [mm]	15.8	7.54	15.8	5.15	15.8	4.66	15.8	4.66	15.8	5.15	15.8	7.54	15.8
L [mm]	15	1.5	7.76	1.5	8.93	1.5	9.08	1.5	8.93	1.5	7.76	1.5	15

Table 3.2: Dimensions for each section in the H-plane filter.

In Fig. 3.3 the S parameters of the filter are shown. Because of the reciprocity theorem [23], only s_{11} and s_{21} must be plotted. Mode-Matching perfectly predicts the resonances for the filter. In FEM, even though a dense mesh was used (around 10k DOFs, half for the symmetric simulation), the results are not as precise, although very satisfactory. When using the axial symmetry formulation, a slightly better result is obtained. It is important to note that this formulation allows the designer to halve the DOFs without reducing the overall accuracy. A comparison of all methods is shown in 3.3d, where "MM" means *Mode-Matching*, "FEM", *regular formulation* and "sym", *using axial symmetry*.

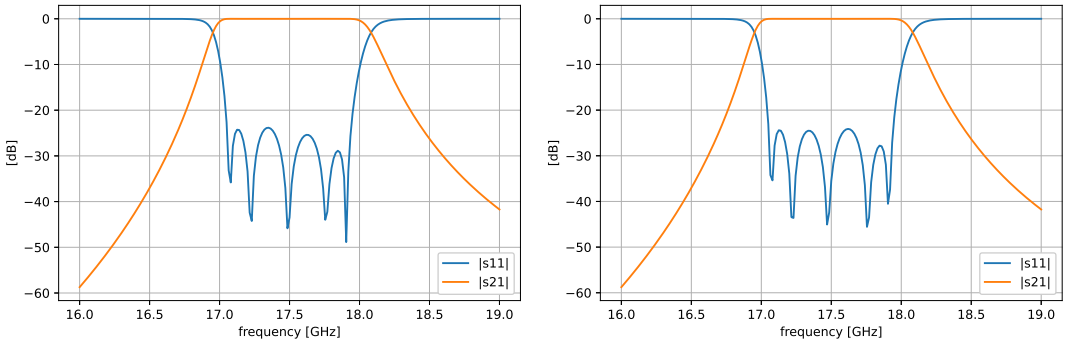

(a) Regular formulation.

(b) Using axial symmetry.

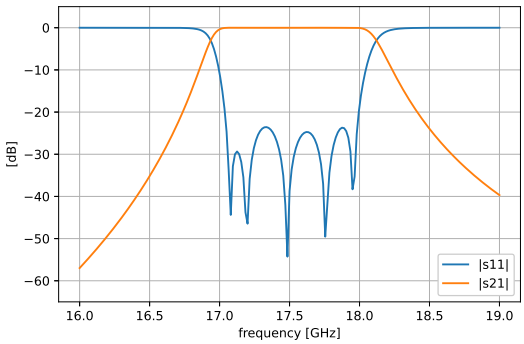

(c) Mode-Matching.

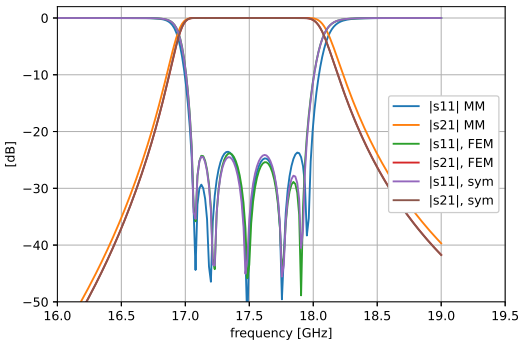

(d) Comparison.

Figure 3.3: Filter s_{ij} parameters.

When applying the symmetry exploitation, only half the structure must be simulated as in shown in Fig. 3.4b. As seen in Fig. 3.4a expected, the magnitude of the field is an even function, thus why PMC must be imposed. This is because the absorbing boundary conditions for the incoming filed are an even function.

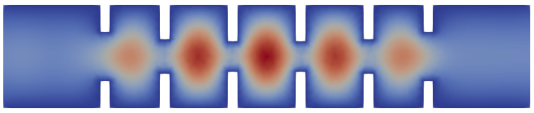

(a) Regular formulation.

(b) Using axial symmetry.

Figure 3.4: Magnitude of the field at the central frequency of the simulation.

3.2.2 E-plane

As an example of the E-plane formulation, a low-pass filter, shown in Fig. 3.6 has been simulated. The filter is also composed of discontinuities, but in this case of a varying height instead of width. The dimensions of each of the sections is shown in Table 3.3, where W, H and L are respectively *width*, *height* and *length*.

E-plane filter, W=42.82mm												
H [mm]	19.41	14.59	39.21	14.59	42.24	14.59	42.24	14.59	39.21	14.59	19.12	22
L [mm]	20	5.45	6.12	15.9	4.14	8.17	4.14	15.90	6.12	0.93	21.35	20

Table 3.3: Dimensions for each section in the E-plane filter.

The results in Fig. 3.5 show a comparison between both simulations also compared against a mode-matching procedure of the same structure. In Fig. 3.5d all results are plotted against each other. Note that both "FEM" and "sym", regarding the computations with and without symmetry are overlapping. Both structures were simulated with Lagrange elements of order 2 with around 10k DOFs (half for the symmetric simulation).

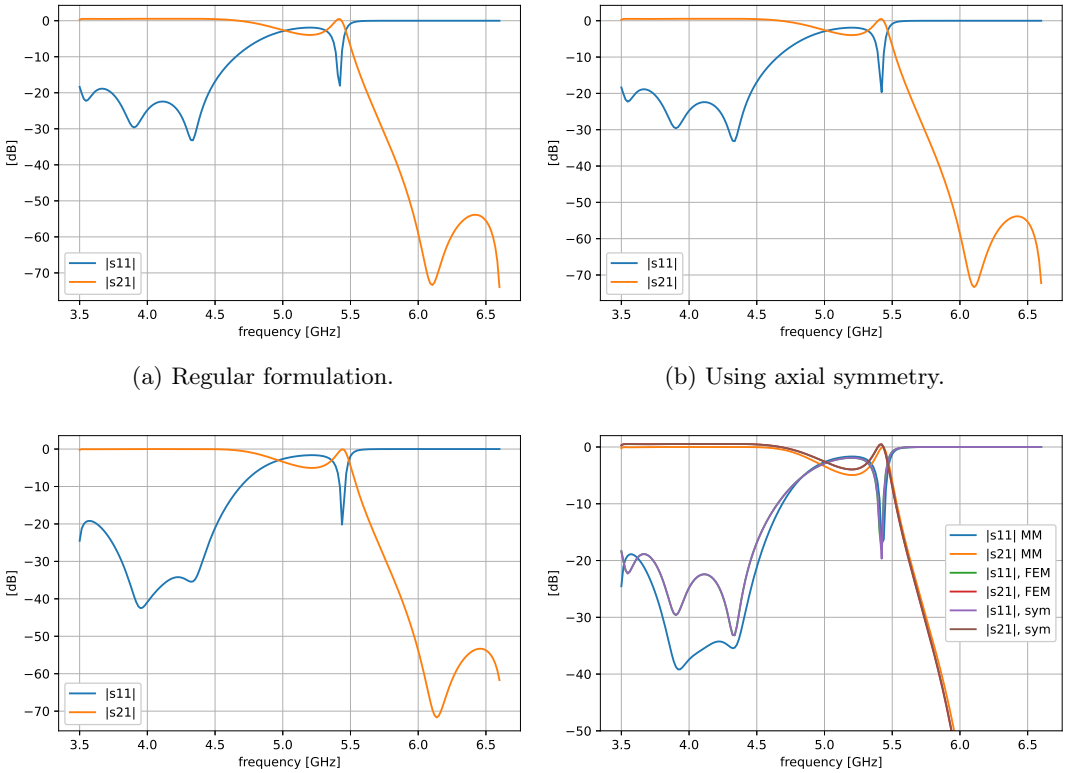

(a) Regular formulation.

(b) Using axial symmetry.

(c) Mode-Matching.

(d) Comparison.

Figure 3.5: Filter s_{ij} parameters.

The modulus of the transmitted h_x field is plotted at the 5GHz frequency in both cases. It can be seen how the field has even symmetry along the longitudinal axis and how the results in Fig. 3.6a are identical to the ones obtained in Fig. 3.6b, thus proving that the tailoring procedure effectively works in both H and E-plane cases.

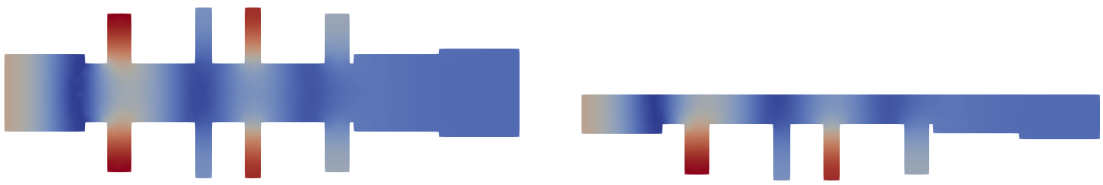

(a) Regular formulation.

(b) Using axial symmetry.

Figure 3.6: Magnitude of the field at 5GHz.

4

One-dimensional scattering formulation

Scattering on periodic structures is another boundary-value problem, similar to what was presented in the previous chapter, with the difference that in this case a unit cell is simulated instead of the whole structure. This is possible thanks to periodic boundary conditions.

4.1 Scattering on periodic structures along the propagation axis

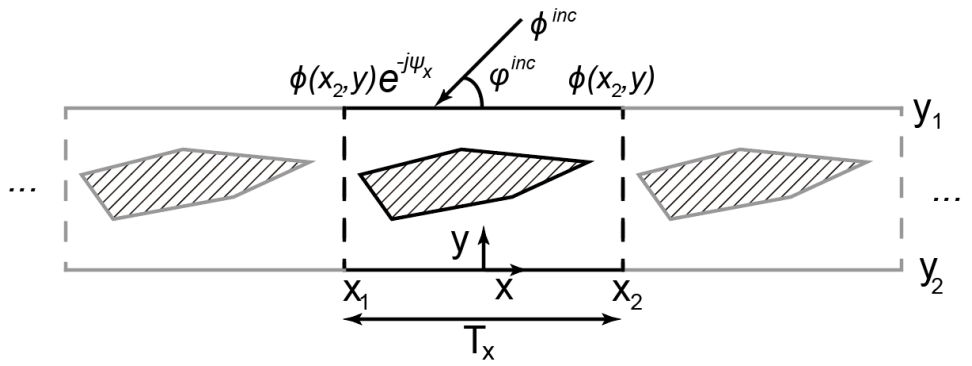

Figure 4.1: Generic periodic structure.

To study scattering in periodic structures we will consider an approach from another author [8], which proposes a more compact formulation than the one presented in the previous section. The method used here is also based on FEM and analytic absorbing boundary conditions at the top and bottom facets (hybrid method). When dealing with periodic structures such as the one presented in Fig. 4.1 it is needed to resort to Floquet's theorem. We consider the incident field a plane wave ϕ^{inc}. Depending on the orientation of the incident vector, it is considered TE or TM. In the first case $\phi = H_z$, and in the second one $\phi = E_z$:

$$\phi^{inc}(x,y) = e^{-j\left(k_x^{inc}x + k_y^{inc}y\right)} = e^{jk_0\left(x\cos\varphi^{inc} + y\sin\varphi^{inc}\right)}, \tag{4.1}$$

where k_0 is the propagation constant in the vacuum. Applying Floquet's theorem [31] we can expand the total field inside the unit cell in terms of the incident field and an infinite sum of

terms called *Floquet harmonics*:

$$\phi(x,y) = \phi^{inc}(x,y) + \phi_p^{sc}(x,y)e^{-jk_x^{inc}x} = \phi^{inc}(x,y) + \sum_{m=-\infty}^{\infty} \tilde{\phi}_{p,m}^{sc}(y_1)e^{-j[k_{xm}x + k_{ym}(y-y_1)]}, \quad (4.2)$$

where

$$\tilde{\phi}_{p,m}^{sc}(y_1) = \frac{1}{T_x}\int_{T_x} \left[\phi(x,y_1) - \phi^{inc}(x,y_1)\right] e^{-jk_{xm}x}dx \quad (4.3)$$

The sum term refers to the scattered field at y_1 and the Floquet harmonics in which it can be decomposed. The constants that appear in the expression above take the values:

$$k_{xm} = -\left(k_0 \cos\varphi^{inc} + \frac{2\pi m}{T_x}\right) \quad (4.4)$$

$$k_{ym} = \begin{cases} \sqrt{k_0^2 - k_{xm}^2}, & k_0^2 \geq k_{xm}^2 \\ -j\sqrt{k_{xm}^2 - k_0^2}, & k_0^2 \leq k_{xm}^2. \end{cases} \quad (4.5)$$

To obtain the final system of equations one has to take the weak form of the Helmholtz formula and impose the absorbing boundary conditions on the left side. On the right side, the excitation vector must be set. Thus, the linear system of equations can be expressed in the following manner:

$$(\mathbf{F} + \mathbf{C})\mathbf{v} = \mathbf{b}, \quad (4.6)$$

Matrices $\mathbf{F}$ and $\mathbf{C}$ conform the functional and are related, respectively, to the Helmholtz equation and the absorbing boundary conditions at the top and bottom facets:

$$F_{ij} = \iint_{\Omega} \left(\frac{1}{u_r}\nabla\alpha_i \cdot \nabla\alpha_j - k_0^2 v_r \alpha_i \alpha_j\right) d\Omega, \quad (4.7)$$

$$C_{ij} = T_x \sum_{m=-\infty}^{\infty} jk_{ym}\left(\tilde{\alpha}_{im,1}^{*}\tilde{\alpha}_{jm,1} + \tilde{\alpha}_{im,2}^{*}\tilde{\alpha}_{jm,2}\right), \quad (4.8)$$

where $u_r = \epsilon_r, v_r = \mu_r$ for TE modes and $u_r = \mu_r, v_r = \epsilon_r$ for TM modes. The term $\tilde{\alpha}_{im,l}$ is computed by obtaining:

$$\tilde{\alpha}_{im,l} = \frac{1}{T_x}\int_{T_x} \alpha_i(x,y_l)\, e^{jk_{xm}x}dx. \quad (4.9)$$

The right-side vector is associated to the derivative on the incident field at the facet located in $y = y_1$. Note the expression is very similar to the one in (4.9), associated to Floquet harmonics.

$$b_i = -j2k_y^{inc}e^{-k_y^{inc}y_1}\int_{T_x} \alpha_i e^{-jk_x^{inc}x}dx. \quad (4.10)$$

To enforce periodicity in the facets at $x = x_1$ (with indices i) and $x = x_2$ (with indices j), we will assume aligned nodes (i.e., all pairs have the same y coordinate). If that is the case the periodic boundary conditions may be applied by performing the following operations:

$$\begin{aligned} &K_{il} \leftarrow K_{il} + K_{jl}e^{-\Psi_x}, \\ &K_{li} \leftarrow K_{li} + K_{lj}e^{\Psi_x}, \\ &\text{Delete the rows/columns} \quad K_{jl}, K_{lj} \\ &b_i \leftarrow b_i + b_i e^{-\Psi_x Tx} \\ &\text{Delete the entries} \quad b_j \end{aligned}$$

where $\Psi_x = k_x^{inc} T_x$ and $\leftarrow$ means assignation. Ψ_x is the phase difference between facets. Using this formulation, the matrix associated to the functional is not hermitian. Applying absorbing boundary conditions worsens the matrix sparsity by filling entries in the rows and columns corresponding to the nodes at the top and bottom facets. The infinite sum in (4.8) must be truncated to M terms. The upside of this formulation is that it allows to take into account any number of Floquet harmonics without increasing the matrix size. Once $\mathbf{v} \cong \phi$ has been obtained the reflection and transmission coefficient of the incident plane wave is:

$$R = \frac{1}{T_x} \int_{T_x} \left[\phi(x, y_1) - \phi^{inc}(x, y_1)\right] e^{jk_x^{inc} x} dx \tag{4.11}$$

$$T = \frac{1}{T_x} \int_{T_x} \phi(x, y_2) e^{jk_x^{inc} x} dx \tag{4.12}$$

Reflection and transmission coefficients of Floquet harmonics may be obtained in a similar manner.

4.2 Scattering devices

In scattering devices there is no direct way of imposing axial symmetry conditions, since, if it is done on the x axis excitation will be duplicated and if it is done on the y axis there is no clear way of imposing periodic boundary conditions. To show how the formulation works, a simple problem of a FSS has been simulated. The problem consists on the incidence of a TM plane wave into an array of cylinders of diameter $d = 1.6$mm and separated $a = b = 4$mm between them. The unit cell chosen is one centered on two cylinders, with the top and bottom boundaries separated another 4mm from the center of the cylinders. This selective structure can be seen in Fig. 4.2.

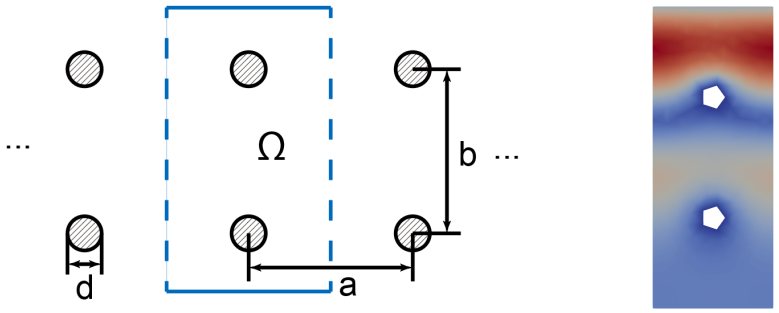

(a) Problem.

(b) Magnitude ot the field at 20 GHz.

Figure 4.2: Problem and implementation using the Finite Element Method.

When dividing in finite elements, circles must be simplified to other kinds of structures, in this case pentagons, as in seen in Fig. 4.2b, where the module of the field is also plotted at 20 GHz with a perpendicular, $\varphi^{inc} = 90°$ incident wave for the dimensions given. The frequency response of the problem can be seen in 4.3, showing the squared module of the reflection coefficient. Results are coherent with was given by the author in [8], with a clear resonance at 16 GHz.

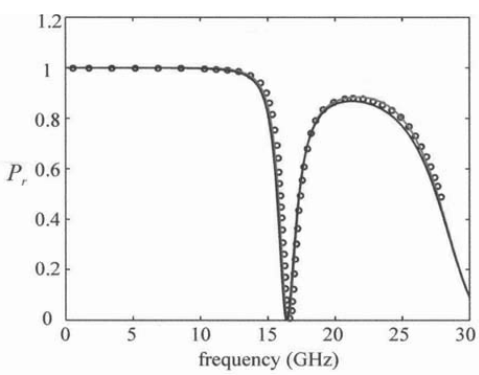

(a) Solution in [8] $\varphi^{inc} = 90°$.

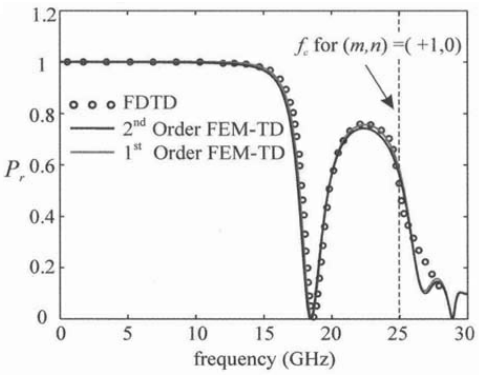

(b) Solution in [8] $\varphi^{inc} = 90°$.

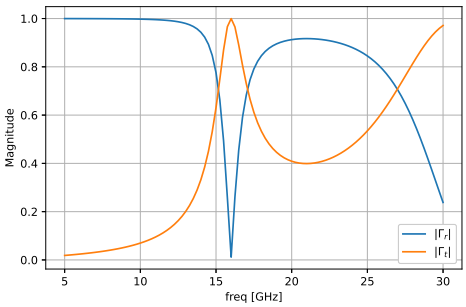

(c) Solution (this work), $\varphi^{inc} = 90°$.

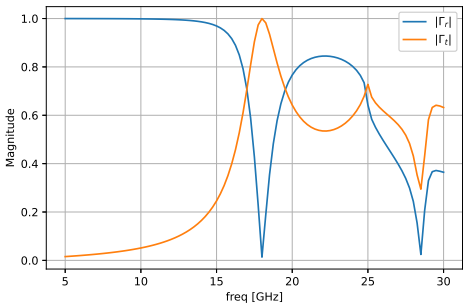

(d) Solution (this work), $\varphi^{inc} = 60°$.

Figure 4.3: Frequency response of the reflection coefficient.

The FEniCS implementation finds great agreement with the results presented in the book. Note that, as frequency increases, the results start being less accurate as the mesh density becomes higher relative to the wavelength. The structure was simulated at around 2500 DOFs and $M = 20$ coefficients.

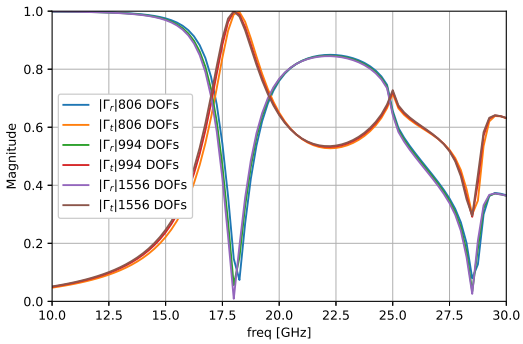

Figure 4.4: Convergence for the case $\varphi = 60°$.

Finally, the effect of tuning the amount of DOFs is shown in Fig. 4.4, where the same structure was simulated with around 800, 1000 and 1500 degrees of freedom. Increasing the DOF count translates into more precise values, especially at the function minima and maxima. It also produces a slight frequency shift due to having more accurate boundaries.

5

Waveguide modal computation

Modal computation does not constitute an excitation problem, such as the ones presented in the previous Chapters. Instead, it is a generalized eigenvalue problem, with infinite eigenvalues and eigenvectors. In this case, no excitation is applied to the problem, since the objective is to analyse its general behaviour. The formulation presented in this chapter is a novel contribution of this work.

5.1 Homogeneous waveguide modal computation

The general theory of transverse electrical (TE) transverse magnetic (TM) modes for homogeneous waveguides enclosed by perfect conductor (as seen in Fig. 5.1a) can be found in [25, 23]. As a brief summary for the part required in this work, the complete set of TE and TM modes for a homogeneous waveguide enclosed by a perfect metallic conductor with a generic cross-section D, is obtained from the solution ψ of the Helmholtz equation $\Delta\psi + k_c^2\psi = 0$, where Δ is the laplacian operator, with the following boundary conditions:

$$\left.\frac{\partial\psi}{\partial n}\right|_{c_\sigma} = 0 \quad \text{for TE modes,} \tag{5.1}$$

$$\psi|_{c_\sigma} = 0 \quad \text{for TM modes,} \tag{5.2}$$

where $\hat{n}$ is the direction normal to the contour c_σ of the cross-section. The total electromagnetic field is obtained from ψ by using the following expressions [23, 31], where ψ represents the longitudinal magnetic field H_z for TE modes (ψ_h) and the longitudinal electric field E_z for TM modes (ψ_e), in a similar manner of the other formulations presented in this Chapter. The remaining components of the field can be obtained by computing, for TE modes:

$$\vec{H}_t = \pm\Gamma e^{\pm\Gamma z}\nabla_t\psi_h, \tag{5.3}$$

$$H_z = -\nabla_t^2\psi_h e^{\pm\Gamma z} = k_c^2\psi_h e^{\pm\Gamma z}, \tag{5.4}$$

$$\vec{E} = \pm Z_h\hat{z}\times\vec{H}_t; \tag{5.5}$$

and for TM modes:

$$\vec{E}_t = \pm\Gamma e^{\pm\Gamma z}\nabla_t\psi_e, \tag{5.6}$$

$$E_z = -\nabla_t^2\psi_e e^{\pm\Gamma z} = k_c^2\psi_e e^{\pm\Gamma z}, \tag{5.7}$$

$$\vec{H} = \mp Y_e\hat{z}\times\vec{E}_t. \tag{5.8}$$

Obtaining the modes of homogeneous waveguides is a problem very well suited for a 2D-FEM approach. It was the first ever electromagnetic problem solved through FEM, as presented by P. Silvester in 1969 [32]. Electromagnetic fields in homogeneous waveguides must satisfy the Helmholtz equation in the domain Ω, which can easily be translated to a variational form by multiplying by the test function v and integrating by parts:

$$\iint_\Omega (v\nabla_t^2\psi + vk_t^2\psi)d\Omega = \iint_\Omega (-\nabla_t v\nabla_t\psi + k_t^2 v\psi)d\Omega + \int_l \frac{\partial\psi}{\partial n}vdl = 0, \tag{5.9}$$

where l is the domain contour and n is the outward normal direction. The line integral vanishes because the function v is required to vanish at the points where ψ is known. With this information, it is now possible to state the consequent generalized eigenvalue problem:

$$\mathbf{Sv} = k_c^2\mathbf{T} \tag{5.10}$$

where $\mathbf{S}$ and $\mathbf{T}$ are the common FEM matrices that have already been discussed in great depth through this work. Indices (i, j) have been moved to superscripts for the sake of clarity in the following expressions:

$$S^{(i,j)} = \iint_\Omega \nabla_t\alpha^{(i)}\cdot\nabla_t\alpha^{(j)}d\Omega \quad [N_{dof}\times N_{dof}]\,, \tag{5.11}$$

$$T^{(i,j)} = \iint_\Omega \alpha^{(i)}\alpha^{(j)}d\Omega \quad [N_{dof}\times N_{dof}]\,. \tag{5.12}$$

5.1.1 Tailoring the formulation for first and second-order symmetries

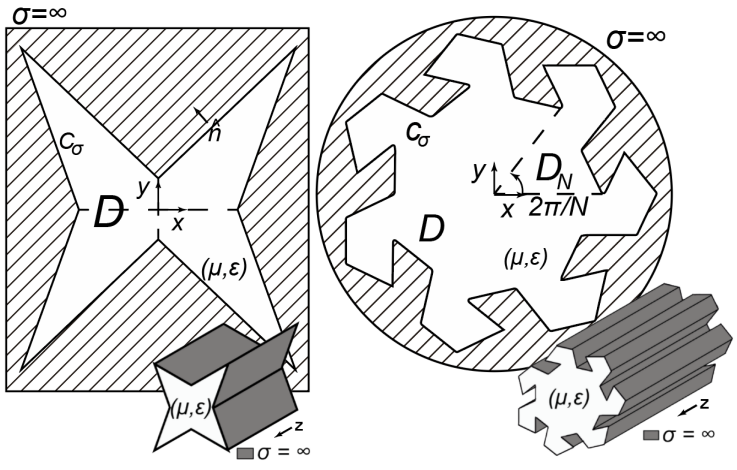

Figure 5.1: (a) Generic cross-section with two-fold axial symmetry (also with C_2 symmetry in the example). (b) Generic C_N cross-section (C_7 in the plotted example, with no planes of axial symmetry) and one of the possible domains D_N to be used for its mode spectrum characterization by the proposed formulation.

To exploit first-order axial symmetry properties designers must impose either Dirichlet or Neumann boundary conditions (PEC or PMC) on the axial plane or planes of the waveguide cross section. The results of each of the problems will yield a set of modes that fulfil these conditions, with the complete set being the union of all of the possible subgroups. This approach does not require any changes from the formulation perspective and is widely used today. For this reason, it will not be discussed any further. It is important to note that this strategy is limited to structures with axial symmetry and cannot be improved beyond the two-fold case. The main objective of the following section will be to extend this concept to the discrete rotational C_N [33] symmetry by an angle of $2\pi/N$ radians, where N is a positive integer, not necessarily 2 or 4 as in the classic one or two symmetry planes case.

C_N rotationally symmetric homogeneous waveguides

The TE and TM modes of closed and homogeneous waveguides with C_N symmetry can be made to satisfy the following equation, which shows a relationship in cylindrical coordinates between slices of the same angular width in their cross-section, given a polar cylindrical reference system (ρ, ϕ, z) fixed on the circumcenter of the structure [33].

$$\psi\left(\rho, \varphi + \tfrac{2\pi}{N}, z\right) = e^{-q\frac{j2\pi}{N}} \psi\left(\rho, \varphi, z\right). \tag{5.13}$$

This relationship shows that to obtain the modes of a structure with rotational symmetry of order N it is only needed to analyse a wedge D_N of $2\pi/N$ radians, thus reducing N times the domain. This well-known result [34, 35] is the basis of the novel specific FEM-based formulation that has been designed for this problem, exploiting the concept of rotational periodic boundary conditions in the cross-section contour. An example of a C_7 waveguide cross-section is shown in Fig. 5.1(b), with a possible reduced domain D_7 that could be employed to compute the modes using this method.

The variable q is an integer that can be defined in the range $\lfloor -N/2 \rfloor < q \leq \lfloor N/2 \rfloor$, where $\lfloor \cdot \rfloor$ represents the floor function. Defining q within these limits allows for an intuitive way of obtaining degenerated modes, the reason for this being that if a value of q is found that satisfies the equation (5.13), then the value $-q$ will satisfy it as well and the fields obtained in both solutions will be complex conjugates [33]. The value of q will be referred to as "mode class" since it determines the family of modes that will be derived, in an analogous way of the sets that appear when enforcing perfect electric and/or magnetic boundaries (PEC/PMC, respectively) in axial symmetry planes.

C_N-FEM modal computation

The equations presented in (5.10) and matrices in (5.11) and (5.12) had to be computed in the whole cross-section D. The C_N symmetry can be exploited to reduce the computational domain to a fraction of the original problem so that $\Omega = D_N$. The expression presented in (5.13) allows for a very loose formulation of the C_N problem, such as the one shown in Fig. 5.2(a). Boundaries can be chosen arbitrarily and may be curvilinear, as long as the angular gap between curves is $2\pi/N$ rad. The remaining edges of the structure must have closed waveguide boundary conditions, typically PEC or PMC depending on the modes that are to be obtained.

Taking this into account, a more specific sketch designed for FEM simulation is presented in Fig. 5.2(b), which shows a slice of a generic C_N cross-section with straight boundaries for rotational symmetry, different from Fig 5.2(a) but without loss of generality, by assuming, for the sake of simplicity and only for visualization purposes, triangular elements with first-order

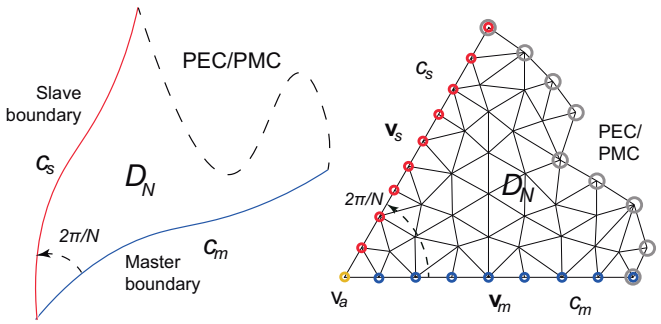

(a) (b)

Figure 5.2: (a) Problem definition and (b) generic FEM implementation.

interpolatory polynomial functions. It is possible to identify the DOFs for the nodes in the edges of the structure, in this case arranged in vector $\mathbf{v}_m$ for the nodes in the lower or *master* [26, 27] boundary c_m, vector $\mathbf{v}_s$ for the nodes in the contour angularly shifted $2\pi/N$ radians from the reference, i.e. *slave* boundary c_s, and v_a for the node at the rotational axis. Please note that, at the mesh level, the number of elements in c_m and in c_s are not restricted at this moment by any relation. In fact, in Fig. 5.2(b) 9 nodes can be spotted in c_m and 10 nodes in c_s. The PEC or PMC boundary conditions have to be applied to the remaining edge nodes, including the nodes that belong to both the conductor and the periodic boundaries. We can define the desired function in these facets and establish the relationship between them according to (5.13):

$$\psi_m = \sum_{i=1}^{M} v_m^{(i)} \alpha_m^{(i)} \quad \text{in } c_m, \tag{5.14}$$

$$\psi_s = \sum_{i=1}^{S} v_s^{(i)} \alpha_s^{(i)} \quad \text{in } c_s, \tag{5.15}$$

$$\sum_{i=1}^{S} v_s^{(i)} \alpha_s^{(i)} = \sum_{i=1}^{M} v_m^{(i)} \alpha_m^{(i)} e^{-q\frac{j2\pi}{N}}, \tag{5.16}$$

where S and M are the total number of nodes at the slave and master facets respectively. Note that in this expression every $\phi_m^{(i)}$ is first projected onto c_s. There will be R remaining nodes in the system, so that $N_{dof} = R + S + M + 1$ (the latter one accounting for the node at the rotational axis.) A Galerkin approach can be applied to (5.16) to seek the relationship between $\mathbf{v}_s$ and $\mathbf{v}_m$:

$$\int_{c_s} \alpha_s^{(j)} \sum_{i=1}^{S} v_s^{(i)} \alpha_s^{(i)} dl = \int_{c_s} \alpha_s^{(j)} \sum_{i=1}^{M} v_m^{(i)} \alpha_m^{(i)} e^{-q\frac{j2\pi}{N}} dl. \tag{5.17}$$

We can obtain the final relationship to be used in the numerical implementation by arranging (5.17) in matrix form with column vectors $\mathbf{v}_s$ and $\mathbf{v}_m$:

$$\mathbf{v}_s = e^{\frac{-j2\pi q}{N}} \mathbf{P}_{ss}^{-1} \mathbf{P}_{sm} \mathbf{v}_m, \tag{5.18}$$

where the real matrices $\mathbf{P}_{ss}$ and $\mathbf{P}_{sm}$ have the following entries with indices i, j:

$$P_{ss}^{(i,j)} = \int_{c_s} \alpha_s^{(i)} \alpha_s^{(j)} dl \quad [S \times S], \tag{5.19}$$

$$P_{sm}^{(i,j)} = \int_{c_s} \alpha_s^{(i)} \alpha_m^{(j)} dl \quad [S \times M]. \tag{5.20}$$

Note that if the nodes are radially aligned (i.e. are at the same radial distance from the node corresponding to v_a) $\mathbf{P}_{ss}^{-1}\mathbf{P}_{sm} = \mathbf{I}_M$, where $\mathbf{I}_M$ refers to an identity matrix of dimensions $M \times M$. It is now possible to display the relationship between all the DOFs in the system such as the one presented in Fig. 5.2(b) and its reduced version without the DOFs at the slave boundary, in a similar fashion as the one proposed in [8] for linearly-shifted periodic boundary conditions used to analyse structures under Floquet-mode excitation:

$$\begin{bmatrix} \mathbf{v}_r \\ \mathbf{v}_m \\ v_a \\ \mathbf{v}_s \end{bmatrix} = \begin{bmatrix} \mathbf{I}_R & \mathbf{0} & \mathbf{0} \\ \mathbf{0} & \mathbf{I}_M & \mathbf{0} \\ \mathbf{0} & \mathbf{0} & e^{\frac{-j2\pi q}{N}} \\ \mathbf{0} & e^{\frac{-j2\pi q}{N}}\mathbf{P}_{ss}^{-1}\mathbf{P}_{sm} & \mathbf{0} \end{bmatrix} \begin{bmatrix} \mathbf{v}_r \\ \mathbf{v}_m \\ v_a \end{bmatrix} = \mathbf{P}\tilde{\mathbf{v}} \tag{5.21}$$

Here, the subscripts a, m and r refer respectively to the DOFs corresponding to the node at the rotation axis, the nodes at the master facet and the remaining nodes of the system. The final number of unknowns is $R+M+1$. The node at the axis requires a special treatment since it actually belongs to both periodic facets, and for that reason has to be present in the reduced system. This complex matrix $\mathbf{P}$ of size $[N_{dof} \times (R+M+1)]$ is utilised to obtain the reduced eigenvalue problem (order $R+M+1$) by multiplying it with matrices $\mathbf{S}$ and $\mathbf{T}$ from (5.11), (5.12), though it is emphasized that the integration domain is now $\Omega = D_N$:

$$\left(\mathbf{P}^H\mathbf{S}\mathbf{P} - k_c^2\mathbf{P}^H\mathbf{T}\mathbf{P}\right)\tilde{\mathbf{v}} = \mathbf{0}, \tag{5.22}$$

$$\left(\mathbf{S}_{red.} - k_c^2\mathbf{T}_{red.}\right)\tilde{\mathbf{v}} = \mathbf{0}, \tag{5.23}$$

where the superscript H refers to the Hermitian (complex conjugate transpose) operation. Once $\tilde{\mathbf{v}}$ has been obtained, $\mathbf{v}$ is easily derived using (5.21). As many of the operations performed in the previous equations are redundant, an efficient implementation may assemble the reduced matrices $\mathbf{S}$ and $\mathbf{T}$ directly, without performing a step by step implementation of the process described above [8]. If we define $\mathbf{P}_p = \mathbf{P}_{ss}^{-1}\mathbf{P}_{sm}$, $\theta = 2\pi q/N$ and:

$$\mathbf{S} = \begin{bmatrix} \mathbf{S}_{rr} & \mathbf{S}_{rm} & \mathbf{S}_{ra} & \mathbf{S}_{rs} \\ \mathbf{S}_{mr} & \mathbf{S}_{mm} & \mathbf{S}_{ma} & \mathbf{S}_{ms} \\ \mathbf{S}_{ar} & \mathbf{S}_{am} & S_{aa} & \mathbf{S}_{as} \\ \mathbf{S}_{sr} & \mathbf{S}_{sm} & \mathbf{S}_{sa} & \mathbf{S}_{ss} \end{bmatrix}, \tag{5.24}$$

then the operation above yields:

$$\mathbf{P}^H\mathbf{S}\mathbf{P} = \begin{bmatrix} \mathbf{S}_{rr} & \mathbf{S}_{rm} + \mathbf{S}_{rs}\mathbf{P}_p e^{-j\theta} & \mathbf{S}_{ra}e^{-j\theta} \\ \mathbf{S}_{mr} + \mathbf{P}_p^T e^{j\theta}\mathbf{S}_{sr} & \mathbf{S}_{mm} + e^{j\theta}\mathbf{P}_p^T\mathbf{S}_{sm} + \mathbf{S}_{ms}e^{-j\theta} + \mathbf{P}_p^T\mathbf{S}_{ss}\mathbf{P}_p & \mathbf{S}_{ma}e^{-j\theta} + \mathbf{P}_p^T\mathbf{S}_{sa} \\ e^{j\theta}\mathbf{S}_{ar} & e^{j\theta}\mathbf{S}_{am} + \mathbf{S}_{as}\mathbf{P}_p & S_{aa} \end{bmatrix} \tag{5.25}$$

If the nodes are aligned:

$$\mathbf{P}^H\mathbf{S}\mathbf{P} = \begin{bmatrix} \mathbf{S}_{rr} & \mathbf{S}_{rm} + \mathbf{S}_{rs}e^{-j\theta} & \mathbf{S}_{ra}e^{-j\theta} \\ \mathbf{S}_{mr} + e^{j\theta}\mathbf{S}_{sr} & \mathbf{S}_{mm} + e^{j\theta}\mathbf{S}_{sm} + \mathbf{S}_{ms}e^{-j\theta} + \mathbf{S}_{ss} & \mathbf{S}_{ma}e^{-j\theta} + \mathbf{S}_{sa} \\ e^{j\theta}\mathbf{S}_{ar} & e^{j\theta}\mathbf{S}_{am} + \mathbf{S}_{as} & S_{aa} \end{bmatrix} \tag{5.26}$$

It becomes obvious that having aligned nodes allows for a more efficient computation, which only needs $2RM+2R+2M^2+2M$ complex multiplications and $2RM+6M$ complex sums. Both values may be halved if matrix $\mathbf{S}$ is hermitian. Looking at (5.25) there is a way of reducing the number of operations while keeping the DOF adjustment. It is done by performing the following

operations, where $i, j = 1, ..., N_{dof}$:

$$\mathbf{S}_{mj} \leftarrow \mathbf{S}_{mj} + e^{j\theta}\mathbf{P}_p^T\mathbf{S}_{sj}, \tag{5.27}$$

$$\mathbf{S}_{im} \leftarrow \mathbf{S}_{im} + \mathbf{S}_{is}\mathbf{P}_p e^{-j\theta}, \tag{5.28}$$

$$\mathbf{S}_{aj} \leftarrow e^{j\theta}\mathbf{S}_{aj}, \tag{5.29}$$

$$\mathbf{S}_{ia} \leftarrow \mathbf{S}_{ixa}e^{-j\theta}, \tag{5.30}$$

$$\text{Remove the rows/columns corresponding to } \mathbf{S}_{sj}, \mathbf{S}_{is}. \tag{5.31}$$

It is important to note that this method yields complex eigenfunctions when $q \neq 0$ and $q \neq N/2$ if N is even. When simulating C_N structures it is desirable to skip the computation of the modes corresponding to negative values of q, since it is known they will exist and have the exact same cutoff wavenumber as their positive counterparts, and their modal electromagnetic fields will be complex conjugates. This actually means every mode of the $q \neq 0$ (and $N/2$ if N is even) family will be degenerated [36]. We offer proof that the previous assertions still hold for the proposed discretized C_N-FEM formulation in Section 5.1.1, contrary to general-purpose FEM where known degenerate modes are split (either when solving for the whole cross-section or imposing different PMC/PEC boundary conditions in axial symmetry planes). This implies that to obtain a complete set of modes only $\lfloor N/2 \rfloor + 1$ eigenvalue problems need to be solved with the proposed C_N-FEM, thus compensating for the need of using complex algebra to solve the cases $q \neq 0, N/2$, as only real algebra is needed for the general-purpose FEM implementation.

Building the projection matrices $\mathbf{P}_{ss}$ and $\mathbf{P}_{sm}$

To build the projection matrix let us first explore the expressions again describing their entries:

$$P_{ss}^{(i,j)} = \int_{c_s} \alpha_s^{(i)} \alpha_s^{(j)} dl \quad [S \times S] \,.$$

This first matrix is a fairly standard FEM matrix that can be computed without much trouble, as it consists on line integrals of the base functions along a contour. On the other hand, matrix $\mathbf{P}_{sm}$ becomes more challenging to build and requires further discussion:

$$P_{sm}^{(i,j)} = \int_{c_s} \alpha_s^{(i)} \alpha_m^{(j)} dl \quad [S \times M] \,.$$

Since the basis functions for both facets are not located in the same contour, the master boundary must first be projected onto the slave boundary. In our case, no way was found to implement it using FEniCS, and was done manually using a procedure that will now be explained. We take the simplest possible example for the sake of clarity, which is a 1D straight line and Laplacian elements of polynomial order 1. For a segment in the interval $[0, 1]$ we have basis functions with the shape:

$$\alpha_1 = \lambda, \tag{5.32}$$

$$\alpha_2 = 1 - \lambda. \tag{5.33}$$

We can compute the integrals relating to the reference segment, in order to use the approach described in 2.1.4, (2.13).

$$\int_0^1 \alpha_1\alpha_1 d\lambda = \int_0^1 \alpha_2\alpha_2 d\lambda = \frac{1}{3}, \tag{5.34}$$

$$\int_0^1 \alpha_1\alpha_2 d\lambda = \int_0^1 \alpha_2\alpha_1 d\lambda = \frac{1}{6}. \tag{5.35}$$

The key idea behind our approach was to obtain the union of the set of points in the master and slave facets projected onto the same line following the procedure shown in Fig. 5.3.

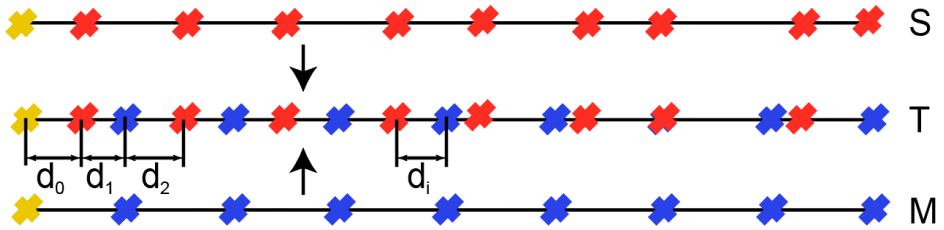

Figure 5.3: Procedure for obtaining the projection matrix.

In the new vector composed of the union of both sets we have $T \leq M + S$ points. For this new vector we may obtain matrix $\mathbf{P}_{tt}$ knowing that the local element matrix is, using the results previously obtained in (5.34), (5.35),

$$\mathbf{P}_{tt}^{[e_i]} = d_i \begin{bmatrix} 1/3 & 1/6 \\ 1/6 & 1/3 \end{bmatrix} \tag{5.36}$$

since the module of the Jacobian $|\mathbf{J}|$ of the transformation is the distance between points d_i. This element matrix can be used to assemble the values into a new matrix of dimensions $S \times M$. Since it is known to which set every point belongs we can do:

1. Compute the matrix $\mathbf{P}_{tt}^{[e_i]}$ for every segment d_i.
2. Find the indices $k, k+1$, $l, l+1$ for the segment in $\mathbf{v}_m$ and $\mathbf{v}_s$ respectively in which d_i is contained.
3. Update the values:

$$P_{sm}^{(k,l)} \leftarrow P_{sm}^{(k,l)} + P_{tt}^{[e_i](1,1)}, \tag{5.37}$$
$$P_{sm}^{(k,l+1)} \leftarrow P_{sm}^{(k,l+1)} + P_{tt}^{[e_i](1,2)}, \tag{5.38}$$
$$P_{sm}^{(k+1,l)} \leftarrow P_{sm}^{(k+1,l)} + P_{tt}^{[e_i](2,1)}, \tag{5.39}$$
$$P_{sm}^{(k+1,l+1)} \leftarrow P_{sm}^{(k+1,l+1)} + P_{tt}^{[e_i](2,2)}. \tag{5.40}$$

This approach is valid because the integral in (5.20) is linear. Performing this task for second order polynomial functions is more laborious since there are three basis functions and matrix $\mathbf{P}_{tt}$ has dimensions $[3 \times 3]$. In this case it is very important to take into account that there are more DOFs than vertices. When performing step 2 in the procedure just explained, indices k and l must be found using the vertices, not the DOFs. The explanation comes again from the equation (5.20) and how the linear combination of segments works. The integrals in this case can be performed with numerical integration.

Proof of degeneracy in C_N-FEM between modes with $\pm q$

Proof of analytical degeneracy between modes obtained for values q and $-q$ can be found in [33]. As this result does not necessarily translate to a numerical formulation, we offer proof that the one presented in this paper also provides the same cutoff wavenumbers for $\pm q$ values and the simple, expected relationship between their eigenvectors. First, recalling from (5.19) and (5.20)

that matrices $\mathbf{P}_{ss}$ and $\mathbf{P}_{sm}$ are strictly real, we establish the relationship between matrix $\mathbf{P}$ in both cases:

$$\mathbf{P}_{-q} = \mathbf{P}_q^*, \quad \mathbf{P}_{-q}^H = \left(\mathbf{P}_q^*\right)^H = \mathbf{P}_q^T, \tag{5.41}$$

where superscript $*$ refers to the complex conjugate and T stands for the transpose operation. For the sake of clarity, let us define the intermediate matrices found in (5.22):

$$\mathbf{A}_q = \mathbf{P}_q^H \mathbf{S} \mathbf{P}_q, \quad \mathbf{B}_q = \mathbf{P}_q^H \mathbf{T} \mathbf{P}_q. \tag{5.42}$$

Now it is possible to rewrite (5.22) for both $\pm q$ cases, and then apply (5.41), taking into account that $\mathbf{S}$ and $\mathbf{T}$ in (5.42) always have real entries:

$$\left(\mathbf{A}_q - k_{c,q}^2 \mathbf{B}_q\right) \mathbf{v}_q = \mathbf{0}, \tag{5.43}$$

$$\left(\mathbf{A}_{-q} - k_{c,-q}^2 \mathbf{B}_{-q}\right) \mathbf{v}_{-q} = \left(\mathbf{A}_q^* - k_{c,-q}^2 \mathbf{B}_q^*\right) \mathbf{v}_{-q} = \mathbf{0}. \tag{5.44}$$

By inspection of these equations we come to the conclusion that $k_{c,q}^2 = \left(k_{c,-q}^2\right)^*$. Since matrices $\mathbf{S}$ and $\mathbf{T}$ are real symmetric as per (5.11) and (5.12), then $\mathbf{A}_q$ and $\mathbf{B}_q$ are Hermitian matrices, namely $\mathbf{A}_q = \mathbf{A}_q^H$, $\mathbf{B}_q = \mathbf{B}_q^H$. This implies both eigenvalues are identical since the mathematical solution of generalized Hermitian eigenvalue problems can only be real. Finally we apply this result to (5.44) and obtain

$$\left(\mathbf{A}_{-q} - k_{c,-q}^2 \mathbf{B}_{-q}\right) \mathbf{v}_{-q} = \left(\mathbf{A}_q - k_{c,q}^2 \mathbf{B}_q\right)^* \mathbf{v}_{-q} = \mathbf{0}. \tag{5.45}$$

Comparing this result to (5.43) yields $\mathbf{v}_{-q} = \mathbf{v}_q^*$, which shows that the eigenvectors are to be complex conjugates. This means the analytical result for analytical C_N modes is maintained in the proposed numerical implementation.

Tailoring the formulation for $C_{N,\nu}$ symmetry

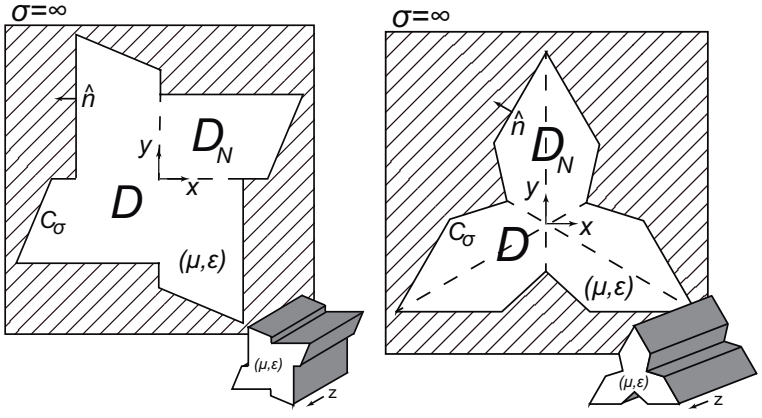

(a) (b)

Figure 5.4: Generic cross-sections (a) C_N (in the figure, C_4); (b) $C_{n,\nu}$, (in the figure, $C_{3,\nu}$.)

This concept, described in [34] refers to waveguides that have axial symmetry planes intersecting along the circumcenter of the structure and are radially spaced π/N rad. In Fig. 5.4 a C_N waveguide is compared against a $C_{N,\nu}$ waveguide. A C_N waveguide is invariant to N different rotations, and a $C_{N,\nu}$ is invariant to N rotations and reflections. It becomes evident that all $C_{n,\nu}$ waveguides are also C_N but not the other way around.

The objective of this section will be to apply Dirichlet boundary conditions to either the real or imaginary part to obtain a better classification of the modes. This theoretically could be done by manipulating the complex system obtained in the previous section, though doing this derives a lack of convergence in the eigensolver. Thus, we first assemble an equivalent system as the one in (5.22) separating the real and imaginary parts, following the procedure shown in Fig. 5.5.

$$\left(\mathbf{P}^H\mathbf{S}\mathbf{P} - k_c^2\mathbf{P}^H\mathbf{T}\mathbf{P}\right)\bar{\mathbf{v}} = \left(\bar{\mathbf{S}} - k_c^2\bar{\mathbf{T}}\right)\bar{\mathbf{v}} = \mathbf{0}, \quad \bar{v}^{(i)} \in \mathbb{C} \tag{5.46}$$

$$\left[\Re\left(\bar{\mathbf{S}} - k_c^2\bar{\mathbf{T}}\right) + j\Im\left(\bar{\mathbf{S}} - k_c^2\bar{\mathbf{T}}\right)\right]\left[\Re\left(\bar{\mathbf{v}}\right) + j\Im\left(\bar{\mathbf{v}}\right)\right] = \mathbf{0} \tag{5.47}$$

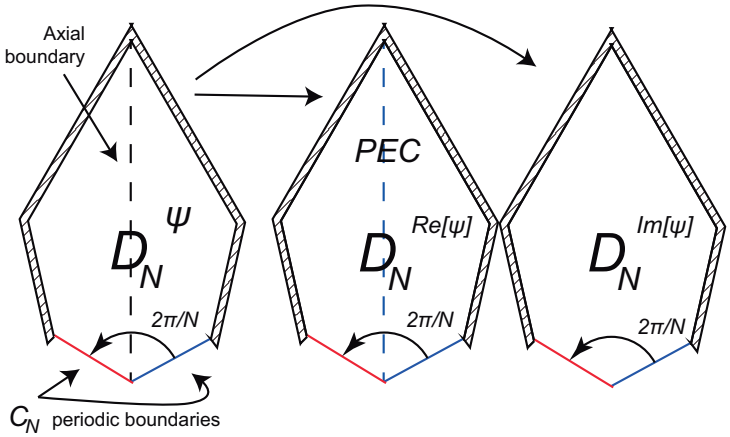

Figure 5.5: Procedure for $C_{N,\nu}$ structures. Conductor facets will be set to PEC or PMC depending on the type of modes that is to be solved (TM or TE).

Now we multiply the terms and put them in matrix form, where $\bar{\mathbf{v}}_{re} = \Re(\bar{\mathbf{v}})$ and $\bar{\mathbf{v}}_{im} = \Im(\bar{\mathbf{v}})$:

$$\left(\begin{bmatrix}\Re\left(\bar{\mathbf{S}}\right) & -\Im\left(\bar{\mathbf{S}}\right)\\ \Im\left(\bar{\mathbf{S}}\right) & \Re\left(\bar{\mathbf{S}}\right)\end{bmatrix} - k_c^2\begin{bmatrix}\Re\left(\bar{\mathbf{T}}\right) & -\Im\left(\bar{\mathbf{T}}\right)\\ \Im\left(\bar{\mathbf{T}}\right) & \Re\left(\bar{\mathbf{T}}\right)\end{bmatrix}\right)\begin{bmatrix}\bar{\mathbf{v}}_{re}\\ \bar{\mathbf{v}}_{im}\end{bmatrix} = (\mathbf{S}_t - k_c^2\mathbf{T}_t)\mathbf{v}_t = \mathbf{0}, \quad \bar{v}_{re}^{(i)}, \bar{v}_{im}^{(i)} \in \mathbb{R} \tag{5.48}$$

At this point it is already possible to apply Dirichlet boundary conditions to either the real or imaginary part in an axial plane. This can be done by:

- Setting the rows in $\mathbf{S}_t$ and $\mathbf{T}_t$ corresponding to those DOFs to 0 except for the values in the diagonals, which are set to 1.
- Removing the rows and columns of $\mathbf{S}_t$ and $\mathbf{T}_t$ corresponding to those DOFs

The second option has been considered the most appropriate choice since it respects the matrices' symmetry and reduces the size of the system. Nevertheless, they produce the same results.

5.1.2 TEM modes in homogeneous waveguides

To obtain the TEM modes in homogeneous waveguides with $C \geq 2$ conductors, the procedure to follow is to solve the Laplace equation for a potential ψ in the domain Ω:

$$\nabla^2\psi = 0. \tag{5.49}$$

Thus the variational problem to be solved is, with the test function v:

$$\iint_\Omega \nabla_t v \nabla_t \psi d\Omega = 0, \tag{5.50}$$

which yields the system $\mathbf{Sv} = \mathbf{0}$, $\mathbf{S}$ being the same matrix as in (5.11). Dirichlet boundary conditions must be set on each on the DOFs associated to the conductors with a fixed value equal to the potential at each one of them. TEM modes obtained with this method are not necessarily orthogonal and the the vectors $\mathbf{v}_i$, $i = 1, ..., C-1$ must be orthogonalised using a method such as Gram-Schimdt.

Obtaining TEM modes with first and second-order symmetries

TEM modes in symmetric structures have even symmetry along their symmetry axes. Thus, in this case, PMC boundary conditions must be enforced at those DOFs. When working with rotational C_N cross-sections, periodic boundary conditions must be imposed with the mode class $q = 0$. This way there will not be any phase difference between points angularly separated $2\pi/N$. In this second case, the PBC are imposed along with the fixed potential values at the conductors. Note that vector $\mathbf{0}$ must have appropriate dimensions according to $\mathbf{S}_{red.}$ from (5.23).

5.2 Waveguide analysis

5.2.1 C_N-FEM computation

To validate the accuracy of the proposed C_N-FEM method, we present a handful of results from various structures with one or none symmetry planes, shown in Fig. 5.6. Please note that with traditional PEC/PMC analysis, these corss-sections only have one or no planes of symmetry, and with the provided formulation, the domain is reduced to $1/N$-th of their section.

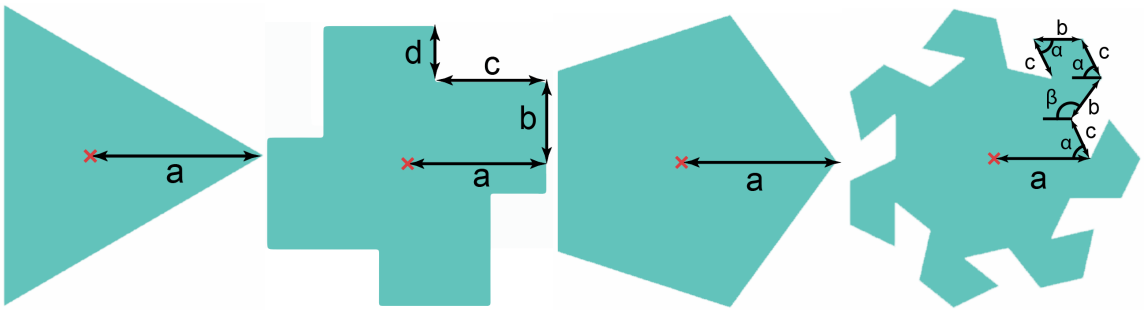

(a) (b) (c) (d)

Figure 5.6: C_N waveguides: (a) C_3 equilateral waveguide, (b) C_4 quadrangular waveguide, (c) C_5 pentagonal waveguide, (d) C_7 shredded waveguide.

To make fair comparisons between structures and procedures some considerations are taken into account. First, the domains D_N have been normalised to have an area of 1 for all structures. Then, 20 TE and TM modes have been computed for each mode class which result in $20(2N-1)$ or $20(2N-2)$ modes in the global scheme if N is odd or even, respectively. Lastly, to compare against general-purpose FEM [7, 8], (i.e. by considering the whole cross-section so that $\Omega = D$ in (5.11) and (5.12) and applying the PEC or PMC boundary condition in the enclosing contour) we simulated with approximately N times the amount of DOFs for the whole structure, as this is approach reasonably takes into account the accuracy gained when using C_N-FEM. These DOFs are always real for the general-purpose FEM and complex for C_N-FEM unless the mode class $q = 0$ or $N/2$ for N even is being computed.

In each table the dimensions and number of DOFs is presented, along with the set of modes identified between brackets "$\{i...j\}$" by propagation order of their mode family corresponding to

their cutoff wavenumber k_c values (with dimensions of inverse of normalized length units.) For general-purpose FEM two rows labelled "A" and "B" are needed for each C_N-FEM row since the general formulation does not guarantee identical k_c for degenerate modes. For waveguides with analytic solutions, degenerate modes have exact equal values, since their k_c are computed with a closed formula.

C_3 Triangular waveguide

First we obtained the cutoff wavenumbers for a waveguide with an analytical solution, in this case an equilateral triangular waveguide in Fig. 5.6a with $a = 1.512$ [37, 38], for which we show the first 2 TE modes for all mode classes and the 20th ones (to show the accuracy). The analytical solution is obtained with the closed formula

$$k_c = \frac{4\pi}{3e}\sqrt{m^2 + n^2 + mn}, \tag{5.51}$$

where e is the length of the side of the isosceles triangle and $m, n \geq 0$ are integers. In this fashion the amount of DOFs was tuned to achieve a relative error of less than 0.15% for the highest-order modes. The results in Table 5.1 show a comparison between the proposed method and the analytical solution, where the fact that the proposed C_N-FEM method is able to discriminate all the degenerate modes is evidenced.

Mode class q	TE 0	TE ±1	TM 0	TM ±1
{1...3} (C_N-FEM)	2.7564	1.5907	2.7569	4.2072
A (analytic)	2.7563	1.5914	2.7563	4.2144
B (analytic)	n/a	same	n/a	same
{4...6} (C_N-FEM)	4.7743	3.1815	5.5130	5.7350
A (analytic)	4.7742	3.1828	5.5128	5.7379
B (analytic)	n/a	same	n/a	same
{7...9} (C_N-FEM)	4.7744	4.2104	7.2940	6.9356
A (analytic)	4.7742	4.2104	7.2927	6.9367
B (analytic)	n/a	same	n/a	same
...	...	...	...	...
{58...60} (C_N-FEM)	14.3566	14.1633	16.8447	16.9014
A (analytic)	14.3226	14.1446	16.7664	16.8418
B (analytic)	n/a	same	n/a	same

Table 5.1: First k_c Values for TE and TM Modes in An Equilateral Triangular Waveguide (C_3) (Fig. 5.6a, $a = 1.512$). DOFs(C_N-FEM)=485.

In the rows named "B" there is either no mode ("n/a") or the cutoff frequency is exactly the same ("same"). Although somewhat redundant, this notation is used for coherency with the rest of the tables.

C_4 Quadrangular waveguide

A cross-section with an even value of N is presented in Fig 5.6b, whose k_c values for TE and TM modes in this case are shown in Table 5.2. Note that in this structure, there are two mode families that are derived with linear polarization and do not have guaranteed degeneracy between any of their modes ($q = \{0, 2\}$). The relative error between methods is inferior to 0.15%, which shows they have a similar convergence given a DOF count ratio proportional to N.

Mode class q	TE 0	TE ±1	TE 2	TM 0	TM ±1	TM 2
{1...4} (C_N-FEM)	3.0015	1.4338	1.8437	2.5149	3.8172	4.4272
A (FEM)	3.0013	1.4339	1.8433	2.51411	3.8176	4.4270
B (FEM)	n/a	1.4339	n/a	n/a	3.8177	n/a
{5...8} (C_N-FEM)	3.8493	3.4562	3.3288	5.0172	5.6804	5.8433
A (FEM)	3.8489	3.4564	3.3287	5.0171	5.6816	5.8411
B (FEM)	n/a	3.4564	n/a	n/a	5.6817	n/a
{9...12} (C_N-FEM)	5.0316	4.1584	4.7483	6.9453	6.9747	6.8305
A (FEM)	5.3105	4.1590	4.7482	6.9446	6.9740	6.8302
B (FEM)	n/a	4.1593	n/a	n/a	6.9743	n/a
...	...	...	...	...	...	...
{77...80} (C_N-FEM)	14.7641	14.5099	14.7789	16.8867	16.9245	16.9034
A (FEM)	14.7529	14.5000	14.7694	16.8701	16.9082	16.8821
B (FEM)	n/a	14.5004	n/a	n/a	16.9098	n/a

Table 5.2: First k_c Values for TE and TM Modes in The Quadrangular Structure in Fig. 5.6b (C_4). $a = 1.2126$, $b = 0.6a$, $c = 0.8a$, $d = 0.4a$ DOFs(C_N-FEM)=532, DOFs(FEM)=2588.

Choosing this DOF ratio will be justified in following sections. Note that the first propagating mode is a TE mode of the mode class $q = 1$ and the first propagating TM mode belongs to the class $q = 0$.

C_5 Pentagonal waveguide

Table 5.3, related to Fig. 5.6c shows the first TE and TM cutoff wavenumbers obtained for a pentagonal waveguide using this technique, which are compared against a classic FEM simulation of the problem using the entire cross-section. In all numerical cases the exact same solver was used, obtaining a relative error of less than 0.1% between them. For simple structures such as this one, lower order modes will have very similar cutoff wavenumbers. For higher order modes this degeneracy becomes less clear as the numbers start to inevitably diverge.

Mode class q	TE 0	TE ±1	TE ±2	TM 0	TM ±1	TM ±2
{1...5} (C_N-FEM)	2.9839	1.4387	2.3051	1.9454	3.0909	4.1178
A (FEM)	4.3257	1.4390	2.3050	1.9452	3.0921	4.1177
B (FEM)	n/a	1.4390	2.3050	n/a	3.0921	4.1177
{6...10} (C_N-FEM)	4.6220	3.8354	3.3819	4.4338	5.5373	5.1468
A (FEM)	4.6216	3.8360	3.3819	4.4325	5.5394	5.1468
B (FEM)	n/a	3.8360	3.3819	n/a	5.5394	5.1468
{11...15} (C_N-FEM)	5.2671	4.5276	5.1658	6.5945	6.1831	6.6928
A (FEM)	5.2672	4.5289	5.1655	6.5945	6.1840	6.6923
B (FEM)	n/a	4.5289	5.1655	n/a	6.1840	6.6923
...	...	...	...	...	...	...
{96...100} (C_N-FEM)	14.7626	14.8846	14.8974	16.1693	16.7524	16.6596
A (FEM)	14.7521	14.8879	14.8945	16.1643	16.7595	16.6588
B (FEM)	n/a	14.8886	14.8956	n/a	16.7633	16.6621

Table 5.3: First k_c Values for TE and TM Modes in A Regular Pentagonal Waveguide (C_5) (Fig. 5.6c), $a = 1.450$. DOFS(C_N-FEM)=489, DOFS(FEM)=2521.

C_7 shredded heptagon waveguide

To show how our model can be applied to all kinds of structures with C_N properties, we finally tested the waveguide of Fig. 5.1b with parameters given in Fig. 5.6d. The results are compared against a classic cross-section simulation using the same solver. In this case $N = 7$, which allows for a reduction of the simulation area of 7 times and allows for 7 different mode classes. Results can be observed in Table 5.4. It can be seen how a general-purpose FEM implementation struggles when obtaining cutoff wavenumbers for degenerate modes in complex structures. The relative error goes up to 0.04%. Note that in this case, because of the complexity of the structure, even lower order degenerate modes start to present disparities in their k_c.

Mode class q	TE 0	TE ±1	TE ±2	TE ±3	TM 0	TM ±1	TM ±2	TM ±3
{1...7} C_N	2.0005	1.0191	1.3418	1.4606	2.0628	3.2715	4.3496	5.2627
A (FEM)	2.0008	1.0193	1.3418	1.4606	2.0644	3.2759	4.3548	5.2730
B (FEM)	n/a	1.0194	1.3421	1.4609	n/a	3.2760	4.3549	5.2733
{8...14} C_N	3.6185	2.5943	3.2819	3.9174	4.6655	5.7601	6.2926	6.3043
A (FEM)	3.6187	2.5950	3.2821	3.9174	4.6714	5.7734	6.3031	3.3095
B (FEM)	n/a	2.5955	3.2825	3.9177	n/a	5.7735	6.3039	6.3101
{15...21} C_N	4.5828	4.3253	4.4803	4.5407	6.4414	6.7278	7.2678	6.8922
A (FEM)	4.5827	4.3259	4.4813	4.5406	6.4494	6.7298	7.2694	6.8921
B (FEM)	-	4.3260	4.4815	4.5408	-	6.7231	7.2695	6.8922
...	...	...	...	...	...	...	...	...
{134...140} C_N	14.5967	14.2501	14.2505	14.5430	16.7121	17.2747	17.3206	17.2453
A (FEM)	14.5929	14.2447	14.2473	14.5382	16.7165	17.2326	17.3149	17.2769
B (FEM)	n/a	14.2460	14.2490	14.5405	n/a	17.2362	17.3162	17.2778

Table 5.4: First k_c Values for TE and TM Modes in The Shredded Waveguide in Fig. 5.1b (C_7) (Also Fig. 5.6d), $a = 1.209$, $b = 0.605$, $c = 0.525$, $\alpha = 5\pi/14$, $\beta = 2\pi/7$. DOFs(C_N-FEM)=525, DOFs(FEM)=3854.

Fields are obtained through the derivative of the eigenvector, and can be shown for this structure in Fig. 5.7. The E filed is plotted in blue and the H field in green.

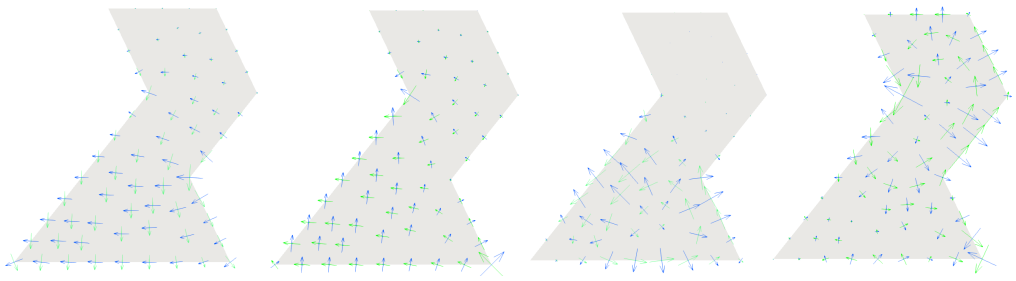

(a) $\Re\{E_t\}$, $\Re\{H_t\}$, (b) $\Im\{E_t\}$, $\Im\{H_t\}$, (c) $\Re\{E_t\}$, $\Re\{H_t\}$, (d) $\Im\{E_t\}$, $\Im\{H_t\}$,

Figure 5.7: First mode in Fig. 5.1(b) (TE, $q = 1$) and third TM mode propagating for $q = 3$.

5.3 Discussion on the C_N-FEM formulation

When computing the fields using the C_N-FEM scheme it becomes very important to take into account that the obtained eigenvectors are complex for mode classes with $q \neq 0$ or $N/2$ if N is even. This, of course, has to be the case since these eigenvectors contain twice the information of the ones obtained through classic FEM as the fields from two degenerate C_N-FEM circularly-polarised modes can be derived from each solution instead of one from each of the two linearly-polarised degenerate classic FEM modes.

5.3.1 Identification of degenerate modes

In all previous tables it was shown how C_N-FEM yields exactly the same cutoff wavenumber for degenerate modes belonging to classes with $\pm q$. To illustrate how this represents a problem in general-purpose FEM, in Fig. 5.8 we show the relative difference between cutoff wavenumbers of degenerate modes in a pentagonal waveguide obtained with general-purpose FEM, simulated with 1300 DOFs. Note that every pair of crosses should be, in the theoretical case, situated in the value 0 for each of the degenerate pairs.

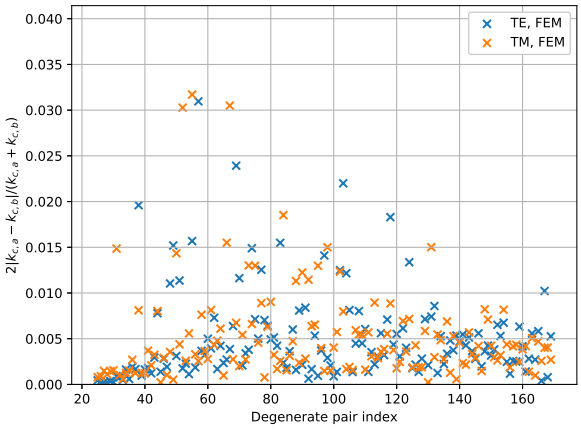

Figure 5.8: Relative difference between k_c of degenerate pairs, pentagonal waveguide.

Indeed, the relative difference, as shown in Fig. 5.8 is not only related to the mesh density and geometry of the structure, but also to the geometry of each of the modes, which is unpredictable. This problem is completely solved using C_N-FEM.

5.3.2 Distribution of C_N-FEM modes

When working with techniques that utilise higher-order modes it is very important to assure no mode has been skipped. C_N-FEM does not skip modes, but we have to check whether all mode classes have the same distribution of modes (i.e. the modes appear at the same rate). In Fig. 5.9 it is shown for each value of k_c^2 the number of modes that have been obtained up to that frequency. It can be seen how it increases linearly with the squared cutoff wavenumber k_c^2, and how the rate of increase is, on average, the same for each mode class. This means that to obtain all modes for a set frequency the same number of modes must be simulated for each mode class. Doing this, there could be some missing modes for the last computed values, and thus the last N or $2N$ computed modes in the whole scheme should be removed to be certain this does not happen.

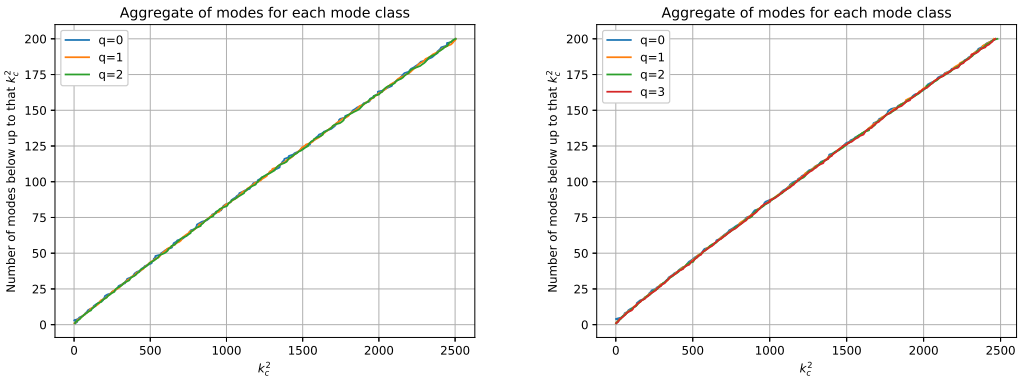

(a) (b)

Figure 5.9: Accumulated modes, (a) pentagonal waveguide, (b) C_7 waveguide.

Another interesting aspect is how the aggregates behave in relation to the structure properties. It has been found that the mean increment of k_c^2 between modes is directly related to the area of the C_N structure D_N. In Fig. 5.10 it can be seen how the mean increment stays the same regardless of the geometry if the area is normalised to the same value for each structure. Note that the whole cross-section area would be N times the area of the C_N wedge. Thus, if the C_N are stays the same, then more more modes overall will appear on the structure the higher N is.

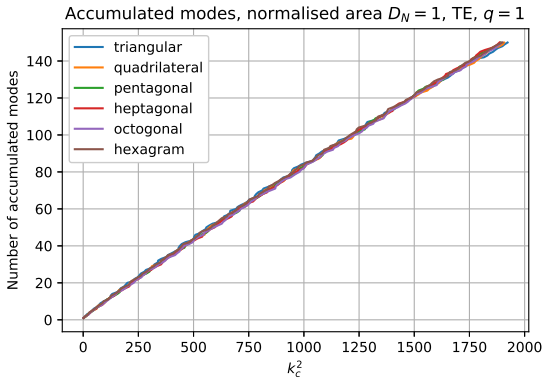

Figure 5.10: Accumulated TE modes for different geometries, $q = 1$.

5.3.3 Convergence of C_N-FEM

The structures with analytical solution also allow us to explore the convergence rate of C_N-FEM in relation to general-purpose FEM by comparing them with the exact cutoff wavenumbers. This can be done by obtaining a figure of merit for the obtained eigenvalues, such as:

$$Err = \frac{1}{N}\sum_{i=1}^{M}\frac{|k^2_{c_i,FEM} - k^2_{c_i,analytical}|}{k^2_{c_i,analytical}} \tag{5.52}$$

where Err is referred to as the mean relative error. It is important to note that, in this case, the mean error will on average be less prominent the lower order the mode is.

To check whether the accuracy is kept equal with the same DOF density (DOFs per unit area), Figs. 5.11a and 5.11b have been obtained, where the DOFs for the general-purpose FEM

formulation have been adjusted by dividing them by 3 and 4 respectively, thus having almost the same density as the C_N-FEM counterpart. It is no surprise to see that the accuracy is very similar when the number of DOFs of general purpose FEM is N times the amount of C_N-FEM DOFs. In 5.11b we can also see how the convergence rate of C_N-FEM and FEM is similar, as proportionally augmenting the DOF count translates into achieving the same reduction in the error function.

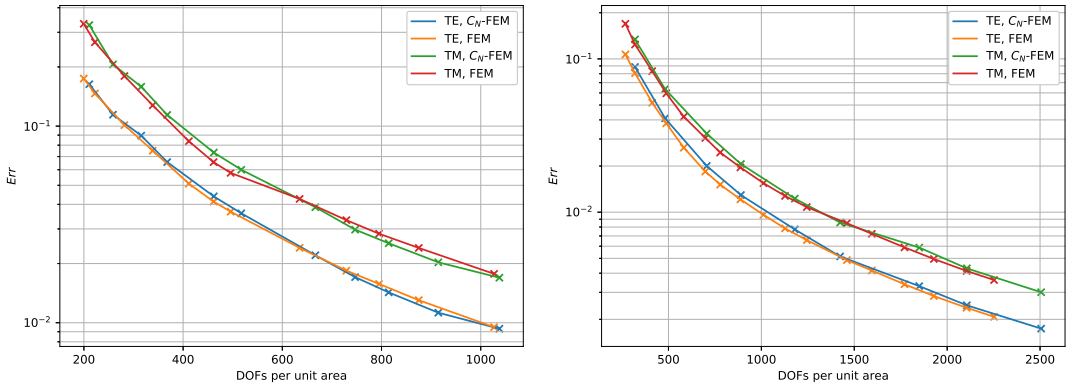

(a) (b)

Figure 5.11: (a) Mean relative error for the triangular waveguide. (b) Same figure with DOFs adjusted to compare DOF density.

5.3.4 Computational cost of C_N-FEM

To obtain the set of the first M TE or TM modes propagating in a waveguide it is only necessary to solve $\lfloor N/2+1 \rfloor$ eigenvalue problems with M/N modes each. This implies solving $M(1/2+1/N)$ modes in the worst case, which represents a halving in the amount of modes to be computed as N increases. On the contrary, because the periodicity condition makes the matrices complex, the eigenproblem for mode classes with $q \neq 0$ and $N/2$ if N is even is complex. This implies an increment in the computation times due to using complex algebra. In addition to this, applying periodic boundary conditions implicates a small overhead due to the matrix multiplications and a decrement on the quality of spares matrices used in the resolution.

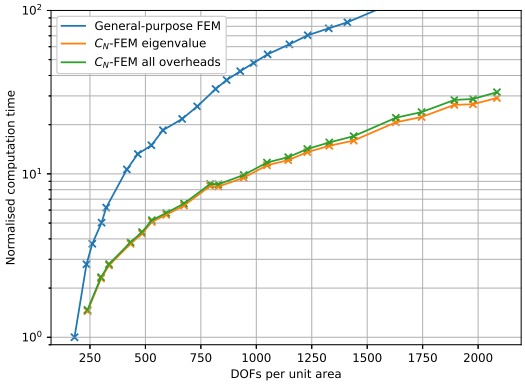

Figure 5.12: Accumulated TE modes for different geometries, $q = 1$.

Performance is quantified in Fig. 5.12, where it is evaluated as computational time normalised to the smallest value of all simulations, presented against DOF count per unit area. In this

example 300 TE eigenvalues were obtained in a triangular waveguide using the same software (ARPACK) in both cases. As expected, the reduction in the DOF count due to the use of a smaller domain prevails over all other overheads that implies utilising C_N-FEM. Note that this is a very conservative case in the performance gain, since better metrics would be obtained for higher N values, which would allow for a greater reduction of the solving domain. For C_N-FEM two curves are included, one showing the time it takes to solve only the eigenvalue problem and another one including the matrix multiplication operations necessary to establish the PBCs.

5.3.5 Circular polarization

The phase shift that the C_N-FEM formulation implies yields modes with complex functions for mode classes $q \neq 0$ and $N/2$ if N is even. These modes can be translated to the ones obtained by general-purpose FEM by performing the operations:

$$\begin{bmatrix} \psi_{FEM_1} \\ \psi_{FEM_2} \end{bmatrix} = \frac{1}{\sqrt{2}} \begin{bmatrix} 1 & 1 \\ -j & j \end{bmatrix} \begin{bmatrix} \psi_{C_N-FEM_1} \\ \psi_{C_N-FEM_2} \end{bmatrix} \tag{5.53}$$

Here the subscript FEM refers to the general-purpose implementation and C_N-FEM the proposed implementation. This transformation is only possible with degenerated modes, but it does not represent a problem because, as stated before, the modes are guaranteed to fulfil that condition. It can be seen this operation is very similar to a transformation from linear to circular polarisation.

Indeed, modes obtained with C_N-FEM are very suitable for circular polarisation. This is because they fulfil rotational boundary conditions. In Fig. 5.13 we show the Axial Ratio and twist direction of modes. The first one (AR) is obtained through orthogonalisation of the real and imaginary parts of the vector:

$$\Psi = \frac{1}{2} \arctan \left(\frac{2\nabla_t \mathbf{v}_r \cdot \nabla_t \mathbf{v}_i}{\nabla_t \mathbf{v}_r \cdot \nabla_t \mathbf{v}_r - \nabla_t \mathbf{v}_i \cdot \nabla_t \mathbf{v}_i} \right) \tag{5.54}$$

$$\vec{\mathbf{b}}_1 = \nabla_t \mathbf{v}_r \cos \Psi + \nabla_t \mathbf{v}_i \sin \Psi \tag{5.55}$$

$$\vec{\mathbf{b}}_2 = -\nabla_t \mathbf{v}_r \sin \Psi + \nabla_t \mathbf{v}_i \cos \Psi \tag{5.56}$$

$$AR = \frac{|\vec{\mathbf{b}}_1|}{|\vec{\mathbf{b}}_2|} \tag{5.57}$$

where $\mathbf{v}_r$ is the real part of the eigenvector $\mathbf{v}$, $\Re\{\mathbf{v}\}$ previously obtained, and $\mathbf{v}_i = \Im\{\mathbf{v}\}$. The twist direction may be obtained through the operation

$$\hat{z} \cdot \left(\vec{\mathbf{b}}_1 \times \vec{\mathbf{b}}_2 \right) \begin{cases} \geq 0, & \text{Counter-clockwise direction,} \\ \leq 0, & \text{Clockwise direction.} \end{cases} \tag{5.58}$$

In Fig 5.13 4 modes the pentagonal waveguide are shown with their respective axial ratio and twist direction, that has been mapped with red in counter-clockwise points and blue in clockwise points. Dots are exactly placed where FEM has computed them. The axial ratio has been limited to 20 dB to better appreciate the variation. The AR computation for every point is especially susceptible of numerical errors in obtaining the gradient of vector $\mathbf{v}$. Nevertheless, the modes that are most suitable to use for circular polarisation are the first propagating ones for each mode class, because they present the least variation.

Finally, circular polarisation can be seen thanks to the power diagram of the structures. A normalised version of the power diagram may be easily obtained by computing:

$$\mathbf{s} = \frac{\nabla_t \mathbf{v} \cdot \nabla_t \mathbf{v}^*}{\max \left(\nabla_t \mathbf{v} \cdot \nabla_t \mathbf{v}^* \right)} \tag{5.59}$$

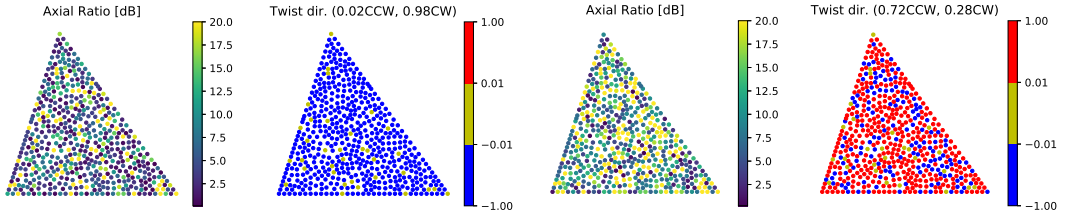

(a) $TE_{0,q=1}$ (b) $TE_{1,q=1}$

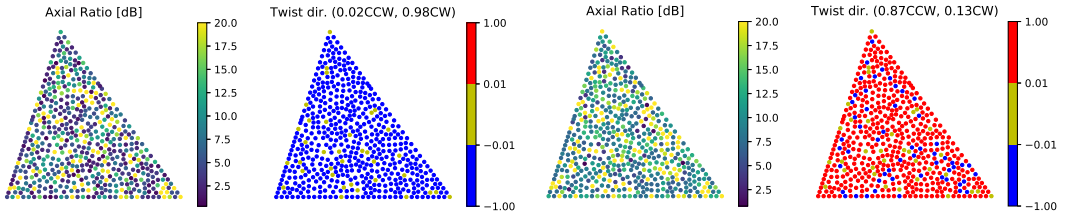

(c) $TE_{0,q=2}$ (d) $TE_{1,q=2}$

Figure 5.13: Axial ratio and twist direction for 4 modes in the pentagonal waveguide (red → CCW (counter clockwise), blue → CW (clockwise.))

In Fig. 5.14 power density is presented for the same modes as in Fig. 5.13, this time with an interpolated visualization in Paraview and for the whole cross-section D. It can be seen how the power diagram has second order rotational symmetry for all modes, a characteristic that is necessary for circular polarisation to be used.

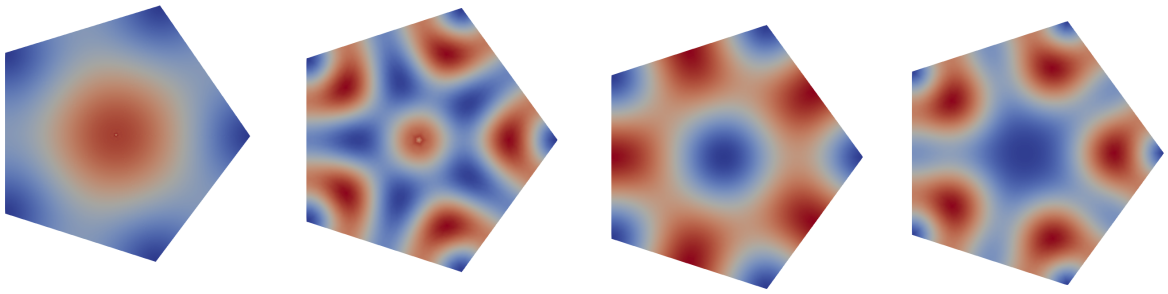

(a) $TE_{0,q=1}$ (b) $TE_{1,q=1}$ (c) $TE_{0,q=2}$ (d) $TE_{1,q=2}$

Figure 5.14: Normalised power diagram for various TE modes in the pentagonal waveguide.

Although the proposed formulation provides proof of degeneracy for modes with values of $q \neq 0$ and $N/2$ if N is even, it is important to note that in some structures, such as the square waveguide, degenerate modes for these other two families exist. In this case, manual inspection of eigenvalues to check for degeneracy is needed since there is no tool available to predict this behaviour. The modes for these two families are obtained with linear polarization using this method (i.e. the phase of the eigenvector is constant). Nevertheless, these modes are never combined when studying circular polarization, so the downsides of this behaviour are limited (or not relevant at all). For the remaining families, the results have a circular polarization that comes from the phase difference enforced in the periodic boundary. This can be an advantage in the context of devices designed to work with circular polarisation, as it is not needed to find and combine linearly-polarised modes to obtain them. On the other hand, we now have to deal

with modes having complex modal functions ψ [39] for the mode classes different from 0 and $N/2$ if N is even.

5.3.6 Mode bandwidth in C_N-FEM

Separating the modes by their rotational symmetry allows for well defined groups that predict propagation and coupling between modes through the waveguide given a certain excitation of one of its modes. This way, if a device is excited with a C_N mode belonging to a class q, in the other end of the structure only modes belonging to that same class will be present. In Table 5.5 the relative percentage bandwidth is shown for various guides defined by regular polygons, obtained using the formula:

$$BW = 2\frac{k_{c,2} - k_{c,1}}{k_{c,2} + k_{c,1}} \tag{5.60}$$

The results are also shown for a 64-sided regular polygon and a circular waveguide (C_∞). It is important to note that this information cannot be obtained directly using general-purpose FEM, since it would require a post-processing for the identification of degenerate modes and the subsequent composition based on their rotational symmetry. It can be observed how the biggest bandwidth appears for the mode class $q = 1$, which is also the one were the fundamental (first propagating) TE mode belongs in the general scheme. The values for the circular waveguide were derived using analytic expressions [23].

Mode class q	N	0	(±)1	(±)2	(±)3	(±)4
Triangle	3	0	66.7	-	-	-
Square	4	34.3	76.4	34.3	-	-
Pentagon	5	42.1	72.9	37.8	-	-
Hexagon	6	44.1	71.7	53.4	17.5	-
Heptagon	7	44.7	71.1	52.2	26.7	-
Octagon	8	45.1	70.8	51.7	42.4	11.3
...	...	...	...	...	...	...
Reg. pol. 64	64	45.8	70.2	50.8	41.2	35.2
...	...	...	...	...	...	...
Circle	∞	45.8	70.2	50.8	41.2	35.2

Table 5.5: Relative monomode bandwidth [%] for various guides defined by regular polygons.

5.3.7 Electromagnetic fields in C_N-FEM in the entire cross-section

If one wishes to obtain the field in the whole original domain, the eigenvector must be rotated geometrically $2\pi/N$ degrees $N-1$ times and have their phases incremented by multiples of $e^{-j2\pi q/N}$. Note that, in general, the electromagnetical fields of a mode do not have rotational symmetry for $q \neq 0$ or $N/2$ if N is even, but the average power density always will. Fig. 5.15 shows the reconstructed E field for the whole structure using a C_N-FEM eigenvector. It has been found that the most numerical errors appear in the acute angles of the structure (the center axis included). Nevertheless, it can be seen how the formulation works exactly as planned.

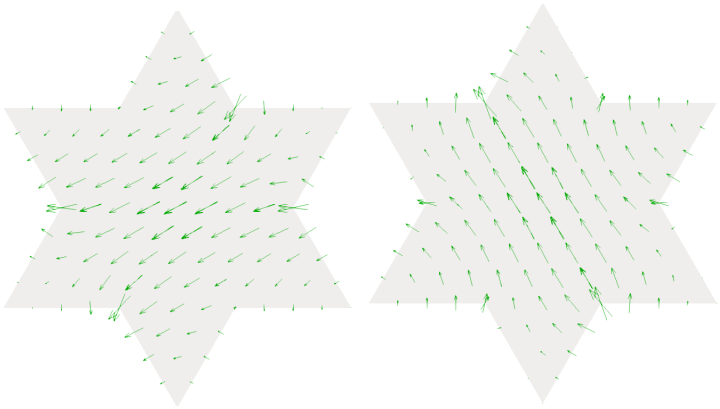

(a) $\Re(\vec{E}), TE_{0,q=1}$ (b) $\Im(\vec{E}), TE_{1,q=1}$

Figure 5.15: $\vec{E}$ for the first propagating mode in a hexagram waveguide.

5.4 Discussion on the $C_{N,\nu}$-FEM formulation

The formulation presented for $C_{N,\nu}$-FEM has the advantages of having the modes categorised not only by their mode class q, but also by having PEC on the real or imaginary part at the reflection axis. In spite of this, it has proven to have an important problem, which is the appearance of undesired spurious modes. We compute the same Table as in 5.1 with the proposed method and obtain the values shown in Table 5.6. What is found is that the spurious modes have the same cutoff wavenumber regardless of the mode class.

Mode class q	TE 0	TE ±1	TM 0	TM ±1
{1...3} ($C_{N,\nu}$-FEM)	2.7564	1.5913	1.1103	1.1103
A (analytic)	2.7563	1.5914	non existent	non existent
{4...6} ($C_{N,\nu}$-FEM)	3.2837	3.1827	2.7564	4.2102
A (analytic)	non existent	3.1828	2.7563	4.2144
{7...9} ($C_{N,\nu}$-FEM)	4.7747	3.2837	5.5138	5.5744
A (analytic)	4.7742	non existent	5.5128	non existent
{10...12} ($C_{N,\nu}$-FEM)	4.7747	4.2107	5.5745	5.7389
A (analytic)	non existent	4.2104	non existent	5.7379
{13...15} ($C_{N,\nu}$-FEM)	4.7747	4.7747	7.2968	6.9394
A (analytic)	4.7742	non existent	7.2927	6.9367
{16...18} ($C_{N,\nu}$-FEM)	5.5138	5.7388	7.2968	7.2968
A (analytic)	5.5128	5.7378	non existent	non existent
...	...	...	...	...

Table 5.6: First k_c Values for TE and TM Modes in An Equilateral Triangular Waveguide ($C_{3,\nu}$) (Fig. 5.6 (a), $a = 1.512$). DOFs($C_{N,\nu}$-FEM)=532.

To further study the origin and properties of the spurious modes a triangular waveguide was simulated, in which different C_N boundaries were tried. They are shown in Fig. 5.16, where A, B, C and D are the different reduced domains and σ the contour along which the Dirichlet

condition was imposed. Area D is the same as A, although in this case σ was chosen to be the same line as one of the C_N boundaries.

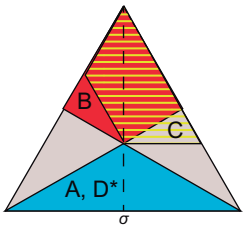

Figure 5.16: Different D_N sections A, B, and C used for simulation.

In Table 5.7 the first TE spurious modes were identified for each of the simulation areas (no mode class is specified since they are identical in all of them). Note that for sections B, C and D they had the exact same cutoff wavenumbers. The only property these reduced areas have in common is that σ was imposed over the "longest" possible symmetry axis, while in A it was imposed on the smallest. Thus, we come to the conclusion that the spurious modes are dependent on where the PEC for the real or imaginary part is set.

Num.	k_c,A	pos.	k_c,B	pos.	k_c,C	pos.	k_c,D	pos.
0	1.760	1	3.284	2	3.283	2	3.284	2
1	4.029	3	4.775	4	4.780	4	4.774	4
2	4.774	5	6.026	6	6.036	6	6.026	6
3	6.246	7	7.295	9	7.309	7	7.295	9
4	7.237	10	7.803	10	7.791	10	7.802	10

Table 5.7: First propagating spurious modes for different areas, TE.

Finally the eigenfunction corresponding to a regular mode and a spurious modes is shown in fig. 5.17 for only a wedge of the structure.

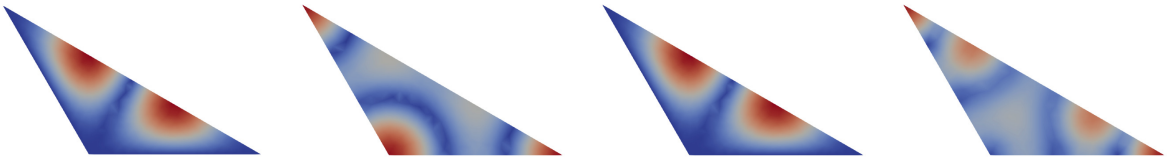

(a) $TE_{4,q=0}$ (b) $TE_{5,q=0}$ (c) $TE_{4,q=1}$ (d) $TE_{5,q=1}$

Figure 5.17: Module of the eigenvector $|\mathbf{v}|$ for various TE modes obtained with the $C_{N,\nu}$ formulation.

It can be seen how not only the eigenvalues are identical for the spurious modes, but the eigenvectors as well. It was found that the relationship between $\text{TE}_{4,q=1}$ and $\text{TE}_{4,q=0}$ is a phase difference of $2\pi/3$. It can also be observed how, for spurious modes, the eigenvector has module 0 on the bisector and both rotational boundaries. This can be a tool to identify spurious modes.

5.4.1 Identifying spurious modes

Identifying modes for mode classes $q = 0$ and $N/2$ for N even is trivial, since all the eigenvectors should be pure imaginary if PEC was set to the real part. Thus, by just checking the module of the real part of the solution it is possible to identify 100% of all spurious modes for these classes, regardless of the mesh. This is not really needed as both of these classes can be solved using linear algebra, but is important to note due to being useful for obtaining spurious modes "on purpose". For the rest of modes classes, this procedure does not work and other tools that have been tried to identify them, such as:

- Cross correlation of the real and imaginary part (is high on spurious modes)
- Mean of the module of the eigenvector at the master boundary (should be null)
- Difference between normalised real and imaginary vectors (should be null)
- See if it is solution of the original eigenvalue problem (should be nonzero for spurious modes)
- Minimum of either the real or imaginary part of the eigenvector multiplied by $e^{-q2\pi/N}$ (should be null)
- Normalised normal derivative of the eigenvector at the master boundary (should be 0 for the imaginary part)

All of these criteria are mesh dependent, and thus are not totally reliable. To compare them a ROC (Receiving Operating Curve, typically used to measure performance in classification problems) has been obtained with the false positive ratio and true positive ration for each of them (in Fig. 5.18). Note that it is not a random variable what it is being studied, and that performance will improve the more dense the mesh is, as it can be seen comparing Figs. 5.18a against 5.18b.

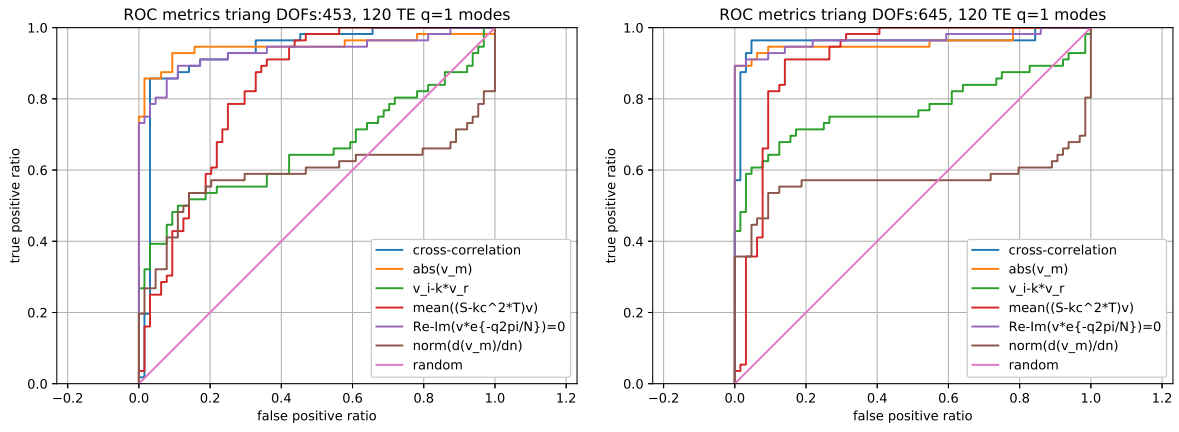

(a) 453 DOFs

(b) 645 DOFs

Figure 5.18: ROC for the various criteria to identify spurious modes (Equilateral triangular waveguide.)

It can be seen that the best strategies are to check for the cross-correlation between the real and imaginary parts, obtain the minimum of the eigenvector multiplied by a phase difference and checking the module of the eigenvector at the master boundary. Nevertheless, they are not completely reliable and because of this it may not be worth to use $C_{N,\nu}$. The performance

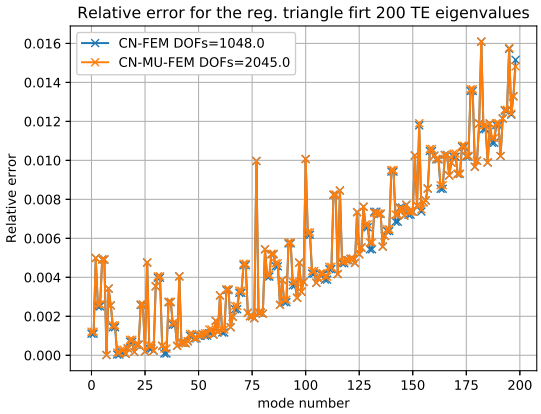

Figure 5.19: $C_{N,\nu}$-FEM accuracy on a mode-by-mode basis against general-purpose FEM and C_N-FEM.

obtained by using $C_{N,\nu}$-FEM is very similar on a mode by mode basis in comparison to C_N-FEM. Both methods yield almost the same results when the number of DOFs is doubled, because C_N-FEM has complex DOFs and $C_{N,\nu}$-FEM has real and imaginary DOFs.

5.5 TEM modes in C_N-FEM and $C_{N,\nu}$-FEM

TEM modes have a cutoff wavenumber $k_c = 0$. Thus, the only interest of obtaining them is to compute the field potential. It does not make sense in this case to use the $C_{N,\nu}$-FEM formulation since the modes are real and it is not necessary to impose any condition on the real or imaginary parts.

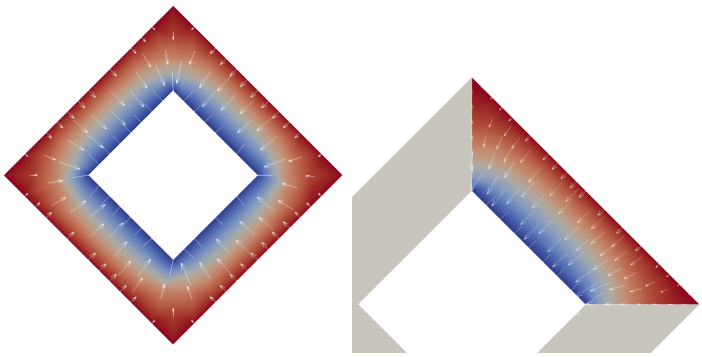

(a) General purpose solution (b) C_N-FEM solution

Figure 5.20: TEM mode of a waveguide made of two squares C_4 and the field $\vec{E}$.

In Fig. 5.20 a simple C_4 structure made of two conductors was simulated. The eigenvector and derived field $\vec{E}$, in white, have been plotted. It can be seen how the solution given by the C_N-FEM TEM formulation described in Section 5.1.2 yields the same result while taking into account only 1/4th of the structure.

6

Conclusions and future work

6.1 Conclusions

Microwave devices are fundamental for the advancement of Information Technology as they constitute the ground in which every communication system is based. In a post Moore's law world, the emphasis is starting to be put in developing optimal strategies for simulation in CAD-oriented design. In this work we have dissected the Finite Element Method, starting from the most basic elements and numerical integration to the resolution on the final linear problems, putting symmetries in the spotlight and establishing relationships between them and the tools used in the Method.

E and H-plane devices have served as a good starting point for the analysis of a solid FEM formulation that was tailored to fit first order symmetry conditions. Scattering problems introduce second-order boundary conditions, and represent another excitation problem that can be optimized using 2D-FEM and scalar elements. Frequency response and convergence were studied for these structures. Modal analysis of closed waveguides is, on the other hand, a generalized eigenvalue problem and has allowed us to make the most progress and optimization using our new symmetry oriented analysis.

In the last case, as more waveguide devices are developed using rotational symmetries as those known as C_N schemes, the use of tailored and efficient simulation tools becomes increasingly desirable. The approach that has been presented, a novel contribution of this work, based on rotational periodic boundary conditions, extends the perfect electric and magnetic conductor analysis for structures with or without axial symmetry, and has been shown to have many advantages. First, it allows for a dimensionality reduction that is more prominent the higher the value of N is, with the only overhead of establishing the rotational periodic boundary condition. Secondly, the use of the mode families categorized by their mode class q value gives mathematical proof of degeneracy for the modes with $q \neq 0$ and $N/2$ if N is even. The presented implementation guarantees the exact same cutoff wavenumber for degenerated modes. Third, the method obtains directly the modes with circular polarisation that will be used in C_N structures composed of several cascaded different C_N waveguides. This is an advantage because it gives information about how the different mode families will be propagating through the structure and predicts mode coupling behaviour, while also providing information about the fields that will be used in polarisers and other devices designed to work with this kind of propagation.

6.2 Future work

In the E and H plane field, there is the possibility of reducing the simulation area even further if the symmetry on the longitudinal axis is taken into account. This is possible thanks to Bartlett's theorem, but was not possible to perform during the project duration due to time constraints.

In scattering devices, it might be possible to take into account symmetries on the perpendicular axis by coupling the boundary conditions into one boundary. This possibility has to be explored in depth, because it introduces some challenges that were out of the scope of the project. There is also the possibility of applying Bartlett's theorem in the longitudinal axis, in a similar way as the one explained for the E and H plane case.

In waveguide devices, as the task of creating a brand new formulation was successfully completed, designing devices utilising it becomes one of the main priorities. There is also the possibility of developing a Mode-Matching formulation that allows the use of complex eigenfunctions, to be used in synergy with the proposed formulation in the analysis of waveguide discontinuities

Another challenge will be to fix the problems presented in the $C_{N,\nu}$ formulation, where spurious modes represent a significant problem. Once a solution has been found, the $C_{N,\nu}$ formulation will surely be more efficient that the current C_N formulation.

Last, but not least, another line of development would be to translate the formulations presented to three dimensions, where the efficiency gains in performance would become even more noticeable.

Acronym Glossary

- **API**: Application Program Interface
- **BC**: Boundary Conditions
- **CAD**: Computer Automated Design
- **DOF**: Degree of Freedom
- **EM**: Electromagnetic
- **FEM**: Finite Element Method
- **FEniCS**: Finite Element Computational Software (Python library)
- **FSS**: Frequency Selective Structure
- **IT**: Information Technology
- **JIT**: Just In Time
- **PBC**: Periodic Boundary Conditions
- **PDE**: Partial Differential Equation
- **PEC**: Perfect Electric Conductor
- **PMC**: Perfect Magnetic Conductor
- **PSS**: Polarization Selective Structure
- **RF**: Radio Frequency
- **ROC**: Receiving Operating Characteristic
- **TE**: Transverse Electric (mode)
- **TEM**: Transverse Electromagnetic (mode)
- **TM**: Transverse Magnetic (mode)
- **UFL**: Unified Form Language
- **WRM**: Weighted Residual Method

Bibliography

[1] Mahdi H. Miraz, Maaruf Ali, Peter S. Excell, and Rich Picking. A review on internet of things (iot), internet of everything (ioe) and internet of nano things (iont). In *2015 Internet Technologies and Applications (ITA)*, pages 219–224, 2015.

[2] Yunlong Cai, Zhijin Qin, Fangyu Cui, Geoffrey Ye Li, and Julie A. McCann. Modulation and multiple access for 5g networks. *IEEE Communications Surveys Tutorials*, 20(1):629–646, 2018.

[3] Galileo satellite system. `https://www.usegalileo.eu/`. Accessed: 2021-06-01.

[4] Spacex's Starlink. `https://www.starlink.com/`. Accessed: 2021-06-01.

[5] K. C. Gupta, R. Garg, and R. Chadha. Computer aided design of microwave circuits. *NASA STI/Recon Technical Report A*, 82:39449, January 1981.

[6] Giuseppe Conciauro. *Advanced modal analysis : CAD techniques for waveguide components and filters*. John Wiley & Sons, 2000.

[7] G. Pelosi, R. Coccioli, and S. Selleri. *Quick Finite Elements for Electromagnetic Waves*. Artech House electromagnetic analysis series. Artech House, 2009.

[8] J.M. Jin. *The Finite Element Method in Electromagnetics*. Wiley - IEEE. Wiley, 2015.

[9] Oskar Zetterstrom, Guido Valerio, Francisco Mesa, Fatemeh Ghasemifard, Martin Norgren, and Oscar Quevedo-Teruel. Mode-matching analysis of loaded transmission lines with twist symmetries. pages 1–5. EurAAP, 2020.

[10] Nataliya Kolmakova, Sergey Prikolotin, Andrey Perov, Vadim Derkach, and Anatoliy A Kirilenko. Polarization plane rotation by arbitrary angle using D-4 symmetrical structures. *IEEE Transactions on Microwave Theory and Techniques*, 64(2):429–435, 2016.

[11] Ginés García Contreras. Trabajo Fin de Grado. Estudio de simetrías no convencionales en guía de onda para su aplicación en dispositivos de comunicaciones con polarización circular, 2019.

[12] Anders Logg and Garth N. Wells. Dolfin: Automated finite element computing. *ACM Transactions on Mathematical Software*, 37(2), 2010.

[13] Martin S. Alnæs, Jan Blechta, Johan Hake, August Johansson, Benjamin Kehlet, Anders Logg, Chris Richardson, Johannes Ring, Marie E. Rognes, and Garth N. Wells. The fenics project version 1.5. *Archive of Numerical Software*, 3(100), 2015.

[14] Anders Logg, Garth N. Wells, and Johan Hake. *DOLFIN: a C++/Python Finite Element Library*, chapter 10. Springer, 2012.

[15] Charles R. Harris, K. Jarrod Millman, Stéfan J. van der Walt, Ralf Gommers, Pauli Virtanen, David Cournapeau, Eric Wieser, Julian Taylor, Sebastian Berg, Nathaniel J. Smith, Robert Kern, Matti Picus, Stephan Hoyer, Marten H. van Kerkwijk, Matthew Brett, Allan Haldane, Jaime Fernández del Río, Mark Wiebe, Pearu Peterson, Pierre Gérard-Marchant, Kevin Sheppard, Tyler Reddy, Warren Weckesser, Hameer Abbasi, Christoph Gohlke, and Travis E. Oliphant. Array programming with NumPy. *Nature*, 585(7825):357–362, September 2020.

[16] Pauli Virtanen, Ralf Gommers, Travis E. Oliphant, Matt Haberland, Tyler Reddy, David Cournapeau, Evgeni Burovski, Pearu Peterson, Warren Weckesser, Jonathan Bright, Stéfan J. van der Walt, Matthew Brett, Joshua Wilson, K. Jarrod Millman, Nikolay Mayorov, Andrew R. J. Nelson, Eric Jones, Robert Kern, Eric Larson, C J Carey, İlhan Polat, Yu Feng, Eric W. Moore, Jake VanderPlas, Denis Laxalde, Josef Perktold, Robert Cimrman, Ian Henriksen, E. A. Quintero, Charles R. Harris, Anne M. Archibald, Antônio H. Ribeiro, Fabian Pedregosa, Paul van Mulbregt, and SciPy 1.0 Contributors. SciPy 1.0: Fundamental Algorithms for Scientific Computing in Python. *Nature Methods*, 17:261–272, 2020.

[17] J. D. Hunter. Matplotlib: A 2d graphics environment. *Computing in Science & Engineering*, 9(3):90–95, 2007.

[18] R.B. Lehoucq, D.C. Sorensen, and C. Yang. *ARPACK Users' Guide: Solution of Large-scale Eigenvalue Problems with Implicitly Restarted Arnoldi Methods*. Software, Environments, Tools. Society for Industrial and Applied Mathematics, 1998.

[19] Robert C. Kirby and Anders Logg. A compiler for variational forms. *ACM Transactions on Mathematical Software*, 32(3), 2006.

[20] Ahrens, James, Geveci, Berk, Law, and Charles. *ParaView: An End-User Tool for Large Data Visualization*. Visualization Handbook. Elsevier, 2005.

[21] Kamal Sarabandi and Nader Behdad. A frequency selective surface with miniaturized elements. *IEEE Transactions on Antennas and Propagation*, 55(5):1239–1245, 2007.

[22] Zhongxiang Shen and Chao Feng. A new dual-polarized broadband horn antenna. *IEEE Antennas and Wireless Propagation Letters*, 4:270–273, 2005.

[23] D.M. Pozar. *Microwave Engineering*. Wiley, 2011.

[24] Anders Logg, Kent-Andre Mardal, Garth N. Wells, et al. *Automated Solution of Differential Equations by the Finite Element Method*. Springer, 2012.

[25] Robert E Collin. *Field theory of guided waves*. John Wiley & Sons, IEEE Press, Piscataway, New Jersey, 1990.

[26] A. A. Tavallaee and J. P. Webb. Finite-element modeling of evanescent modes in the stopband of periodic structures. *IEEE Transactions on Magnetics*, 44(6):1358–1361, 2008.

[27] A. Bostani and J. P. Webb. Finite-element eigenvalue analysis of propagating and evanescent modes in 3-D periodic structures using model-order reduction. *IEEE Transactions on Microwave Theory and Techniques*, 60(9):2677–2683, 2012.

[28] Martin R Stiglitz and Julie Callahan. Waveguide components for antenna feed systems: Theory and cad. *Microwave Journal*, 37(6):147–148, 1994.

[29] Constantine A Balanis. *Advanced engineering electromagnetics*. John Wiley & Sons, Hoboken, New Jersey, 1999.

[30] Jorge A Ruiz-Cruz and Jesús M Rebollar. Eigenmodes of waveguides using a boundary contour mode-matching method with an FFT scheme. *International journal of RF and microwave computer-aided engineering*, 15(3):286–295, 2005.

[31] Robert E Collin. *Foundations for microwave engineering*. McGraw-Hill physical and quantum electronics series. McGraw-Hill, New York, 1966.

[32] P Silvester. Finite element solution of homogeneous waveguide problems. *Alta Frequenza*, 38(1):313–317, 1969.

[33] Sazonov V.P. Silin R.A. *Slow-down Systems*. Soviet Radio, 1966.

[34] P. R. McIsaac. Symmetry-induced modal characteristics of uniform waveguides. In *S-MTT International Microwave Symposium Digest*, volume 74, pages 75–77, 1974.

[35] P. R. McIsaac. Symmetry-induced modal characteristics of uniform waveguides - II: Theory. *IEEE Transactions on Microwave Theory and Techniques*, 23(5):429–433, 1975.

[36] M. Mrozowski. *Guided Electromagnetic Waves: Properties and Analysis*. Computer methods in electromagnetics series. Research Studies Press, 1997.

[37] Brian J. McCartin. Eigenstructure of the equilateral triangle, part II: The Neumann problem. *Mathematical problems in engineering*, 2002(6):517–539, 2002.

[38] Brian J. McCartin. Eigenstructure of the equilateral triangle, part I: The Dirichlet problem. *SIAM review*, 45(2):267–287, 2003.

[39] Gian Guido Gentili, Giuseppe Pelosi, Francesco Piccioli, and Stefano Selleri. On the symmetry of scattering matrix in waveguide circuits. *Microwave and optical technology letters*, 61(2):464–468, 2018.